Three-dimensional earthquake sequence simulations with evolving temperature and pore pressure due to shear heating: Effect of heterogeneous hydraulic diffusivity

Hiroyuki Noda[1] and Nadia Lapusta[2]

Received 13 June 2010; revised 7 September 2010; accepted 27 September 2010; published 10 December 2010.

[1] A new methodology for three-dimensional (3-D) simulations of earthquake sequences is presented that accounts not only for inertial effects during seismic events but also for shear-induced temperature variations on the fault and the associated evolution of pore fluid pressure. In particular, the methodology allows to capture thermal pressurization (TP) due to frictional heating in a shear zone. One-dimensional (1-D) diffusion of heat and pore fluids in the fault-normal direction is incorporated using a spectral method, which is unconditionally stable, accurate with affordable computational resources, and highly suitable to earthquake sequence calculations that use variable time steps. The approach is used to investigate the effect of heterogeneous hydraulic properties by considering a fault model with two regions of different hydraulic diffusivities and hence different potential for TP. We find that the region of more efficient TP produces larger slip in model-spanning events. The slip deficit in the other region is filled with more frequent smaller events, creating spatiotemporal complexity of large events on the fault. Interestingly, the area of maximum slip in model-spanning events is not associated with the maximum temperature increase because of stronger dynamic weakening in that area. The region of more efficient TP has lower interseismic shear stress, which discourages rupture nucleation there, contrary to what was concluded in prior studies. Seismic events nucleate in the region of less efficient TP where interseismic shear stress is higher. In our model, hypocenters of large events do not occur in areas of large slip or large stress drop.

Citation: Noda, H., and N. Lapusta (2010), Three-dimensional earthquake sequence simulations with evolving temperature and pore pressure due to shear heating: Effect of heterogeneous hydraulic diffusivity, *J. Geophys. Res.*, *115*, B12314, doi:10.1029/2010JB007780.

1. Introduction

[2] Active faults experience a wide range of slip rates, from orders of magnitude below the plate rate ($\sim 10^{-9}$ m/s) to coseismic slip rates ($\sim 10^{0}$–10^{1} m/s). Previous modeling work [e.g., *Lapusta et al.*, 2000; *Lapusta and Liu*, 2009] successfully reproduced key features of both seismic and aseismic fault behavior: nucleation and dynamic propagation of a rupture, postseismic slip, and slow slip (or creep) throughout the interseismic period. It considered the behavior of a fault governed by a rate- and state-dependent friction law, embedded in a linearly elastic infinite body, and loaded by a tectonically slow rate, while fully incorporating inertial effects during rapid slip. Such simulations of the entire slip history of a fault showed that the characteristics of dynamic rupture events significantly affect, and sometimes control the overall fault behavior, including the spatiotemporal pattern of seismic slip accumulation, the resulting post- and interseismic slip, the level of stress at which the fault operates, and the net frictional heat generation. Hence it is important, even for simulations of long-term fault slip, to make the descriptions of dynamic events as realistic as possible.

[3] Experimental and theoretical studies of the mechanical behavior of faults have revealed that the fault strength reduces tremendously during rapid slip from what is commonly observed at low slip rates, due to a number of physical processes that depend on the rock type and the fault conditions [e.g., *Sibson*, 1973; *Lachenbruch*, 1980; *Mase and Smith*, 1987; *Tsutsumi and Shimamoto*, 1997; *Andrews*, 2002; *Hirose and Shimamoto*, 2005; *Noda and Shimamoto*, 2005; *Mizoguchi et al.*, 2006; *O'Hara et al.*, 2006; *Rempel and Rice*, 2006; *Rice*, 2006; *Sirono et al.*, 2006; *Han et al.*, 2007; *Mizoguchi et al.*, 2007; *Beeler et al.*, 2008; *Brantut et al.*, 2008; *Noda*, 2008; *Fukuyama and Mizoguchi*, 2010; *Sulem and Famin*, 2009; *Sone and Shimamoto*, 2009]. Many of the mechanisms are activated by frictional heating during

[1]Division of Geological and Planetary Sciences, California Institute of Technology, Pasadena, California, USA.
[2]Division of Geological and Planetary Sciences and Division of Engineering and Applied Science, California Institute of Technology, Pasadena, California, USA.

0148-0227/10/2010JB007780

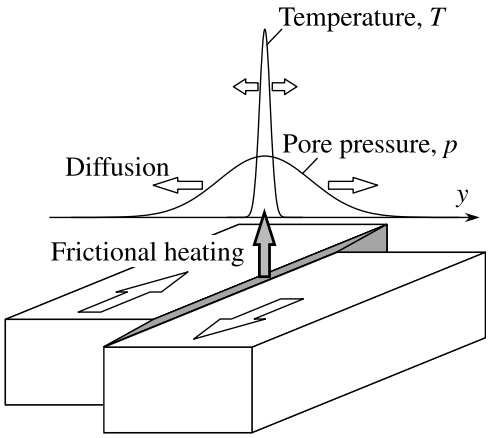

Figure 1. A schematic diagram for thermal pressurization (TP). Shear heating on the fault tends to increase temperature and pore pressure during seismic events. The effectiveness of TP depends on the competition between shear heating and diffusion of heat and fluids off the fault. If TP is efficient, it causes dynamic weakening of the shear zone.

rapid slip characteristic of seismic events, including thermal pressurization of pore fluids (TP), flash heating of the microscopic contacting asperities, and frictional melting [e.g., *Rice*, 2006, and references therein]. The temperature rise in the vicinity of a fault has been studied based on geological observations, including the existence of pseudotachylytes [e.g., *Sibson*, 1975], the change in the ESR signal [*Fukuchi et al.*, 2005], the decomposition and reaction of rock-forming minerals [e.g., *Hirono et al.*, 2008; *Hamada et al.*, 2009a, 2009b], and the recovery of fission tracks [*d'Alessio et al.*, 2003]. It is critically important to incorporate frictional heating and the resulting weakening processes into models of earthquake sequences so that the seismological observations as well as outcomes from field and experimental geology can be properly interpreted.

[4] Here we focus on the thermal pressurization of pore fluids which was first proposed by *Sibson* [1973] to explain the rare occurrence of pseudotachylytes. Coseismically, rapid slip generates heat on a fault, increasing temperature and hence pore pressure if the hydraulic diffusivity of the surrounding rock is sufficiently low (Figure 1). The elevated pore pressure reduces the effective normal stress on a fault, causing dynamic weakening during an earthquake. This mechanism has been considered in studies of dynamic rupture propagation [*Andrews*, 2002; *Noda*, 2004; *Cocco and Bizzarri*, 2004; *Andrews*, 2005; *Bizzarri and Cocco*, 2006a, 2006b; *Suzuki and Yamashita*, 2006; *Noda et al.*, 2009], the quasi-dynamic nucleation of ruptures [*Schmitt and Segall*, 2008], and a long-term cycle simulation of a spring-slider-dashpot model [*Mitsui and Hirahara*, 2009]. Implementing TP into continuum modeling of earthquake sequences is challenging because of the limited numerical resources available and a wide range of spatial and temporal scales that need to be resolved.

[5] In this work, we develop a suitable methodology for incorporating temperature and pressure evolution into earthquake sequence simulations, fully accounting for both inertial effects and dynamic weakening associated with TP during seismic events. The main new development is a spectral method for integrating off-fault diffusion equations for temperature and pore pressure that allows for variable time stepping.

[6] We then apply the newly developed method to simulations of earthquake sequences on a fault with a simple heterogeneity in the hydraulic diffusivity. This is motivated by field studies that show that hydraulic properties are often heterogeneous along faults; they depend on the confining and pore fluid pressures, temperature, chemistry of pore fluid, and local lithology including the type of host rocks and their deformation history [e.g., *Wibberley and Shimamoto*, 2003; *Faulkner and Rutter*, 2003; *Faulkner*, 2004]. *Tanikawa and Shimamoto* [2009] measured hydraulic properties of the fault material collected from boreholes on the Chelungpu fault, Taiwan, a source fault of the 1999 Chi-Chi earthquake. They showed that the hydraulic diffusivity is different by 1 to 2 orders of magnitude between the northern and southern regions of the fault. That is why we consider interaction of two fault patches with potentially different hydraulic diffusivity. Our simulations reveal a number of interesting features, including the resulting complexity of fault slip, different locations for the maximum slip and peak temperature increase, and propensity of earthquakes to nucleate in the patch with less efficient TP, which is contrary to prior studies. We also show that it is important to study the consequences of fault heterogeneity in the context of earthquake sequences.

2. Methodology for Including Temperature and Pore Fluid Pressure Evolution in Long-Term Simulations of Fault Slip

2.1. Problem Formulation

[7] In this study, we extend the methodology of *Lapusta and Liu* [2009] to explicitly include the evolution of temperature T in the shear zone and the associated effects on pore pressure p and fault strength τ. We consider a planar fault embedded in an infinite linear elastic space. The fault is given by $y = 0$ in a Cartesian coordinate system xyz and obeys the following fault constitutive relation (i.e., fault friction),

$$\tau_\alpha = \frac{V_\alpha}{V}\tau\big(V, T(y=0), p(y=0), \theta, \tau_y\big), \tag{1}$$

where $\tau_\alpha(x, z, t)$, $\alpha = x, z$, are the shear stresses on the fault, τ is the frictional strength, $V_\alpha(x, z, t)$ are the components of the slip rate vector, $V = \sqrt{V_x^2 + V_z^2}$ is the magnitude of the slip rate (often called simply "slip rate" in the following), $T(x, y, z, t)$ is the temperature, $p(x, y, z, t)$ is the pore fluid pressure, θ is an additional state variable, and $\tau_y(x, z, t)$ is the normal stress across the fault. Note that we consider only cases with no opening ($V_y(x, z, t) = 0$) and hence the relation (1) applies to the fault at all times.

[8] The temperature and pore pressure evolve due to shear heating on the fault and diffusion off the fault, in the form [e.g., *Lachenbruch*, 1980]

$$\frac{\partial T(x,y,z,t)}{\partial t} = \alpha_{th}\frac{\partial^2 T(x,y,z,t)}{\partial y^2} + \frac{\omega(x,y,z,t)}{\rho c}, \tag{2}$$

and

$$\frac{\partial p(x,y,z,t)}{\partial t} = \alpha_{hy}\frac{\partial^2 p(x,y,z,t)}{\partial y^2} + \Lambda\frac{\partial T(x,y,z,t)}{\partial t}, \quad (3)$$

where α_{th} and α_{hy} are the thermal and hydraulic diffusivities, ρc is the specific heat capacity, Λ is the pore pressure change per unit temperature change under undrained conditions, and ω (x, y, z, t) is the shear heating source. Without loss of generality, T and p are defined as changes from the initial conditions. The shear heating source $\omega(x, y, z, t)$ is caused by fault slip. In the simulated examples, we assume that

$$\omega = \tau V\frac{\exp(-y^2/2w^2)}{\sqrt{2\pi}w}, \quad (4)$$

where w is the half width of the shearing layer that accommodates the slip rate V. Our methodology does not depend on the functional form of ω as long as its Fourier transform, Ω, can be accurately truncated as discussed in section 2.2.

[9] The formulation (2)–(3) neglects the nonlinear terms such as advective heat transfer and heat generation due to compression of pore fluids [*Mase and Smith*, 1987]. *Lachenbruch* [1980] showed that the advective heat transfer was not important in calculating the temperature rise. *Vredevoogd et al.* [2007] examined all terms appearing in the full formulation by *Mase and Smith* [1987] and concluded that the conductive heat and fluid transfer are the dominant terms. The formulation follows previous studies [*Andrews*, 2002; *Bizzarri and Cocco*, 2006a, 2006b; *Noda et al.*, 2009; *Bizzarri*, 2009] in assuming that fault-normal diffusion of heat and pore fluids dominates over the fault-parallel one. This point is justified in section 2.3. We also neglect the effect of inelastic pore volume change (dilatancy and compaction) [e.g., *Segall and Rice*, 1995; *Suzuki and Yamashita*, 2009]. It can be implemented in the numerical calculation if we assume a similar distribution of a sink/source term in the evolution equation for p. Investigation of its effects is beyond the scope of this work and will be pursued in a future study, given the large number of the additional parameters.

[10] One can reformulate equations (2) and (3) to obtain, if $\alpha_{th} \neq \alpha_{hy}$,

$$\frac{\partial(p+\Lambda' T)}{\partial t} = \alpha_{hy}\frac{\partial^2(p+\Lambda' T)}{\partial y^2} + (\Lambda+\Lambda')\frac{\omega}{\rho c}, \quad (5)$$

where $\Lambda' = \Lambda\alpha_{th}/(\alpha_{hy} - \alpha_{th})$.

[11] Following *Lapusta and Liu* [2009], we use a spectral boundary integral equation method (BIEM) to account for elastodynamic effects of fault motion on fault stresses, including inertial effects during rapid seismic events, as explained in section 3.

2.2. Spectral Method for Integrating Equations of Temperature and Pore Pressure Evolution

[12] We have developed a new spectral method to numerically solve equations (2) and (5) which is suitable for simulations of earthquake sequences. Previous studies incorporated effects of the temperature and pore pressure into dynamic rupture propagation with either an explicit finite difference method [*Noda*, 2004; *Noda et al.*, 2009] or a boundary integral equation method (BIEM) [*Bizzarri and Cocco*, 2006a, 2006b]. The former method can deal with changes in physical properties (e.g., water viscosity, permeability and porosity of the rock) but requires short time steps (shorter than the critical value determined by the Courant-Friedrichs-Lewy condition). Thus, it is not applicable to earthquake sequence simulations in which time steps are taken adaptively [*Lapusta et al.*, 2000] to simulate both seismic events and interseismic periods. The BIEM of *Bizzarri and Cocco* [2006a, 2006b] allows for long interseismic time steps, but it requires storage of the time history of the heat generation rate, τV, which makes the calculation much more expensive in terms of computer memory. We use BIEM for the elastodynamic computations, and the time-history storage of V_x and V_z is currently the limiting factor in choosing the model size and resolution. Adding the need to store the time histories related to pore pressure and temperature evolution would significantly reduce the applicability of the methodology, as the shear heating-related time histories required are much longer than the ones we currently store for elastodynamics.

[13] To integrate equations (2) and (5) in time, we first apply a Fourier transformation with respect to y, obtaining

$$\frac{\partial\Theta(x,l,z,t)}{\partial t} = -l^2\alpha_{th}\Theta + \frac{\Omega(x,l,z,t)}{\rho c}, \quad (6)$$

and

$$\frac{\partial(\Pi(x,l,z,t)+\Lambda'\Theta)}{\partial t} = -l^2\alpha_{hy}(\Pi+\Lambda'\Theta) + (\Lambda+\Lambda')\frac{\Omega}{\rho c}, \quad (7)$$

where l spans the wave numbers associated with y, and Θ, Π, and Ω are Fourier transformations of T, p, and ω, respectively. Equations (6) and (7) are no longer partial differential equations, but a couple of independent ordinary differential equations in the form

$$\dot{F}(t) = -AF(t) + B(t), \quad (8)$$

where A does not depend on time. Given the value of $F(t)$, $F(t + \Delta t)$ can be found analytically as

$$F(t+\Delta t) = e^{-A\Delta t}\left(\int_0^{\Delta t} B(t+t')e^{At'}dt' + F(t)\right). \quad (9)$$

Assuming constant $B(t)$ during the time step, we further find

$$F(t+\Delta t) = \frac{B(t)}{A}\left(1 - e^{-A\Delta t}\right) + F(t)e^{-A\Delta t}. \quad (10)$$

We use this analytical solution in our numerical procedure as discussed in section 3. This diffusion solver is unconditionally stable since the numerical error in $F(t)$ always decays exponentially with Δt.

[14] Note that the temperature and pore pressure at the center of the shear zone is given by

$$T(x,0,z,t) = \frac{1}{\sqrt{2\pi}}\int_{-\infty}^{\infty}\Theta(x,l,z,t)dl, \quad (11)$$

and

$$p(x,0,z,t) = \frac{1}{\sqrt{2\pi}} \int_{-\infty}^{\infty} \Pi(x,l,z,t)dl. \quad (12)$$

For an efficient numerical procedure, the support of the shear heating source term, Ω, should be limited in the direction of l. For the shear heating source (4), Ω is given by

$$\Omega = \tau V \frac{\exp(-l^2 w^2/2)}{\sqrt{2\pi}}. \quad (13)$$

Under the adiabatic and undrained conditions, if we restrict the source term to the range $-10/w < l < 10/w$, only 1.5×10^{-23} of the total contribution to $T(x, 0, z, t)$ and $p(x, 0, z, t)$ would be missed. This is well below the round-off error of the double precision. Furthermore, equations (6) and (7) indicate that higher wave number components decay faster, causing further shrinking of the region in the wave number domain where the contribution to $p(x, 0, z, t)$ is nonnegligible. This is a very useful feature for considering the diffusion problems in the wave number domain.

[15] In the numerical implementation, we consider a finite region, $[-|l_e|, |l_e|]$, along the l axis. Note that because of the symmetry about $l = 0$, we consider only the region $[0, |l_e|]$. For the examples with the shear heating source (13), we set $l_e = 10/w$. In earthquake cycle simulations, relevant time scales vary by orders of magnitude, from the subsecond time for elastic waves to propagate over a grid element to multiple earthquake recurrence intervals which are in hundreds of years. Since the time constants in the evolution of Θ and Π are proportional to $1/l^2\alpha_{th}$ and $1/l^2\alpha_{hy}$ (equations (6) and (7)), this variation in time scales motivates discretizing l on a logarithmic scale,

$$\ln\left(l_j(x_i,z_k)\right) = \ln(l_e) + \Delta\ln(l)(N_l - j), (j = 1,2,\ldots,N_l). \quad (14)$$

where x_i, l_j, and z_k are grid points along x, l, and z, $\Delta\ln(l)$ is the logarithmic grid interval, and N_l is the total number of grid points along l axis. The integrations in equations (11) and (12) are calculated using the trapezoidal rule,

$$T(x_i,0,z_k,t) = \sum_{j=1}^{N_l} F^{inv}(j;i,k)\Theta\left(x_i,l_j,z_k,t\right) \quad (15)$$

and

$$p(x_i,0,z_k,t,t) = \sum_{j=1}^{N_l} F^{inv}(j;x_i,z_k)\Pi\left(x_i,l_j,z_k,t\right), \quad (16)$$

where $F^{inv}(j; x_i, z_k)$ is a vector,

$$F^{inv}(j;x_i,z_k) = \begin{cases} \sqrt{2/\pi}l_j(x_i,z_k)(1+\Delta\ln(l)), & j=1; \\ \sqrt{2/\pi}l_j(x_i,z_k)\Delta\ln(l)/2, & j=N_l; \\ \sqrt{2/\pi}l_j(x_i,z_k)\Delta\ln(l) & \text{otherwise.} \end{cases} \quad (17)$$

In the examples, we choose $N_l = 60$ and $\Delta\ln(l) = 0.3$. The numerical error in T and p is then below 10^{-6} relative to their coseismic values, if the other variables are estimated accurately enough, as discussed in section 2.3 and Appendix A. Note that there is no need to calculate the spatial distributions of T and p, to assume periodic conditions in the y direction, or to conduct fast Fourier transforms.

[16] In principle, our method should work for other shapes of the heat source distribution, but further tuning of the wave number grid may be needed for each function. For example, *Fialko* [2004] used a rectangular function, the Fourier transformation of which is a sinc function. The sinc function oscillates around 0 and its envelope decays inversely proportionally to the wave number. Such decay is much slower than that for the Gaussian function. In order to resolve such a slow decay, we would need to consider a much larger domain for l and at least several grid points in each section between zeros which appear regularly in a linear scale. Proper treatment of specific functions deserves further study.

2.3. Comparison With an Analytical Solution for a Prescribed Heat Source

[17] Here we demonstrate that our diffusion solver works well for logarithmically wide range of time scales. A simple relevant example of the temperature and pore pressure evolution is a short-term constant heat input that mimics a coseismic period, followed by a long diffusion that mimics the following interseismic period. Hence let us consider the following heat generation history,

$$\tau V = \begin{cases} (\tau V)_0, & 0 < t < \Delta t_{\min}; \\ 0 & \text{otherwise.} \end{cases} \quad (18)$$

Letting Q stand for either $T\rho c/(\tau V)_0$ or $(p + \Lambda' T)\rho c/((\Lambda + \Lambda')(\tau V)_0)$, we can write equations (2) and (5) with (4) as

$$\frac{\partial Q}{\partial t} = \alpha_* \frac{\partial^2 Q}{\partial y^2} + (H(t) - H(t - \Delta t_{\min}))\frac{\exp(-y^2/2w^2)}{\sqrt{2\pi}w}, \quad (19)$$

where $H(t)$ is the Heaviside step function and α_* is either α_{th} or α_{hy}. The analytical solution for $t > \Delta t_{\min}$ is given by [*McKenzie and Brune*, 1972]

$$Q^{ana}(y,t) = \frac{1}{2\alpha_*}\left[\left[y\sqrt{\frac{\xi}{\pi}}\exp\left(\frac{-1}{\xi}\right) - y\,\mathrm{erfc}\left(\frac{1}{\sqrt{\xi}}\right)\right]_{\xi=\frac{2w^2}{y^2}}^{\xi=\frac{4\alpha_* t' + 2w^2}{y^2}}\right]_{t'=t-\Delta t_{\min}}^{t'=t}, \quad (20)$$

and at $y = 0$, is given by

$$Q^{ana}(0,t) = \frac{1}{2\alpha_*\sqrt{\pi}}\left(\sqrt{4\alpha_* t + 2w^2} - \sqrt{4\alpha_*(t - \Delta t_{\min}) + 2w^2}\right). \quad (21)$$

Figure 2 shows the comparison between the analytical and numerical solutions, $Q^{ana}(0, t)$ and $Q^{num}(0, t)$, normalized by the maximum value of the analytical solution, $Q^{ana}(0, \Delta t_{\min})$, with $\alpha_* = 10^{-4}$ m^2/s which is representative of the values used in this study. The numerical solution compares very well with the analytical solution until about 10^{13} s after heat generation, which is much longer than the typical earthquake recurrence

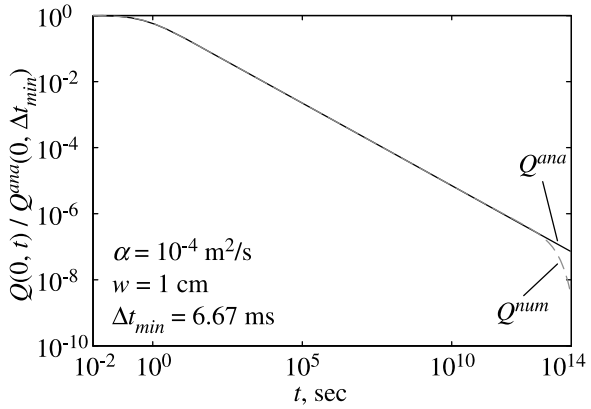

Figure 2. Comparison of numerical and analytical solutions for the diffusion equation (equation (19)). Numerically calculated Q is in good agreement with the analytical solution until about 10^{13} s or 100,000 years, which is long enough compared to the earthquake recurrence intervals.

interval (~tens to hundreds of years or 10^9–10^{10} s). Note that the eventual truncation of the memory effect is caused by the nonzero l_1. α_* ranges from 10^{-6} to 10^{-2} m^2/s in this study, and we have checked the accuracy of the solver for all those values. More detailed error analysis is presented in Appendix A.

[18] This calculation shows that fault-parallel diffusion should not affect the examples presented in the following sections. For the fault-parallel diffusion to manifest itself in the simulation, the diffusion length, $2\sqrt{\alpha_* t}$, should become comparable to the fault-parallel grid spacing, h. We use h = 60 m in this study. $\alpha_* = 10^{-4}$ m^2/s, for example, would result in such diffusion lengths in 10^7 s after a dynamic event which is much longer than the typical event duration. Furthermore, Figure 2 suggests that the value of Q decreases to only 1 percent of the coseismic value at about 10^4 s after an earthquake. Hence the pore pressure or temperature rise on the fault would be dissipated because of the fault-normal diffusion long before the fault-parallel diffusion would have the chance to affect the neighboring fault cell.

3. Numerical Algorithm for the Full Coupled Problem of Fault Slip, Temperature, and Pore Pressure Evolution

[19] In the examples shown in section 4, we assume the following regularized rate- and state-dependent friction law [*Rice et al.*, 2001] with the effective normal stress,

$$\tau = f\sigma_e = a\sinh^{-1}\left(\frac{V}{2V_0}\exp\left(\frac{f_0 + b\ln(\theta/\theta_0)}{a}\right)\right)\sigma_e, \qquad (22)$$

where f is the friction coefficient, a and b are nondimensional rate-and-state parameters, f_0 and θ_0 are the friction coefficient and state variable for the steady state sliding with the reference slip rate V_0, and σ_e is the effective normal stress. We use the standard effective stress law [*Terzaghi*, 1936],

$$\sigma_e = -\tau_y - p(y = 0), \qquad (23)$$

where τ_y is the normal component of the elastodynamic fault traction, positive in tension. The evolution of θ is given by

$$\frac{d\theta}{dt} = \frac{V}{L}(\theta_{ss}(V) - \theta), \theta_{ss}(V) = L/V, \qquad (24)$$

where L is the characteristic slip for the state evolution. This state evolution law is typically called the "aging law"; it incorporates logarithmic time strengthening of a fault [*Dieterich*, 1972, 1979] which is important for simulating interseismic healing.

[20] Note that laws in which friction strength is proportional to the effective normal stress do not always hold in cases of variable effective normal stress. For cases with variable normal stress, *Linker and Dieterich* [1992] proposed an experimentally based law in which a part of the shear stress change in response to a normal stress change is accomplished through gradual evolution and not abruptly. This gradual evolution was shown to be critically important in proper formulations of problems that involve slip between elastically dissimilar materials [e.g., *Cochard and Rice*, 2000]. In the Linker-Dieterich law, the evolution in τ after a change in σ_e is associated with the same characteristic distance, L, as for the evolution effect after a change in V. In this study, we use parameters which result in normal stress changes on slip scales much larger than L (section 4.2), making the evolution in shear stress in response to the evolution in normal stress instantaneous by comparison and allowing us to adopt the formulation (22). The same conclusion was reached by *Noda et al.* [2009] in simulations of single instances of dynamic ruptures with and without the Linker-Dieterich effect, for a different set of thermo-poroelastic parameters than the one used in this work. Hence it appears that normal stress variations due to shear heating may be too slow to require the incorporation of the Linker-Dieterich effect, although we cannot exclude the possibility that this effect would be important in some parameter regimes.

[21] The elastodynamics can be efficiently calculated using spectral BIEM [*Geubelle and Rice*, 1995; *Lapusta et al.*, 2000; *Lapusta and Liu*, 2009]. The traction vector at a point on a fault, $\tau_\alpha(x, z, t)$, = x, y, z, is expressed as

$$\tau_\alpha(x,z,t) = \tau^0_\alpha(x,z,t) + \phi_\alpha(x,z,t) - \eta_\alpha V_\alpha(x,z,t). \qquad (25)$$

In equation (25), τ^0_α is the traction that would act on the fault if it were constrained against any slip or opening, $\eta_x = \eta_z = \mu/2c_s$ and $\eta_y = \mu c_p/2c_s^2$ where μ is the shear modulus, and c_p and c_s are the P- and S wave speeds, respectively. The last term in equation (25), $\eta_\alpha V_\alpha(x, z, t)$, represents radiation damping [*Rice*, 1993]; ϕ_α is a functional term representing the stress transferred by elastic waves. In our calculation, V_y is always zero (e.g., there is no opening or material interpenetration) and hence ϕ_y is always zero as well, so that $\tau_y = \tau^0_y$. Hence, the elastodynamic normal stress does not vary with time, although the effective normal stress that enters friction does vary with time, due to variations in pore pressure. That is why, in the following, the subscripts α and β represent only the fault parallel components, x and z. In the calculation presented in this paper, we set a lower limit to σ_e as 1 MPa.

[22] Following *Lapusta and Liu* [2009], the stress transfer functional ϕ_α is calculated in the spectral domain,

$$\Phi_\alpha(k,m,t) = \int_{t-t_w}^{t} C_{D\alpha\beta}(k,m,t-t')\dot{D}_\beta(k,m,t')dt' + C_{S\alpha\beta}(k,m)D_\beta(k,m,t), \quad (26)$$

where Φ_α, D_α, and $\dot{D}_\alpha$ are 2-D Fourier transforms of ϕ_α, slip δ_α, and V_α, respectively, k and m are coordinates in the wave number domain associated with x and z, $\{C_{D\alpha\beta}\}$ is the matrix of convolution kernels for the dynamic wave propagation, t_w is the length of the time window in which the dynamic wave propagation is accounted for, and $\{C_{S\alpha\beta}\}$ is the matrix for calculating static stress transfers (for details, see *Geubelle and Rice* [1995] and *Lapusta and Liu* [2009]). Note that *Lapusta and Liu* [2009] developed the wave number-dependent truncation for the time convolution in equation (26) which is not used in this work. The integration in equation (26) is estimated by the midpoint rule.

[23] At each discretized time point, we equate equations (1) and (25) to solve for V_α and τ_α with Newton-Raphson method, assuming constant values, integrated over the previous time step, for δ_α, temperature T (or its Fourier transform Θ), pore pressure p (or its Fourier transform Π), and state variable θ. Let us denote the vector containing $V_\alpha(x_i, z_k, t)$ and $\tau_\alpha(x_i, z_k, t)$ by $\mathbf{Y}(t)$, and the vector containing $\delta_\alpha(x_i, z_k, t)$, $\theta(x_i, z_k, t)$, $\Theta(x_i, l_j(x_i, z_k), z_k, t)$, and $\Pi(x_i, l_j(x_i, z_k), z_k, t)$ by $\Psi(t)$. Suppose we know $\mathbf{Y}(t_n)$, $\mathbf{\Psi}(t_n)$, and $\dot{D}_\alpha(t)$ ($t \le t_n$). Our goal is to obtain the values of all variables at the time $t_{n+1} = t_n + \Delta t$, where the time step Δt is calculated using the same considerations as those of *Lapusta and Liu* [2009] (section 4.2).

[24] Let us introduce the following formalism that will allow us to show that our updating procedure can be considered as a predictor-corrector scheme. Integration of Ψ from $\hat{t}$ by $\Delta\hat{t}$ using certain known values, $\mathbf{Y}_c$ and Ψ_c, can be expressed in the following general form:

$$\Psi(\hat{t}+\Delta\hat{t}) = \chi^{\Delta\hat{t}}(\mathbf{Y}_c, \Psi_c) \circ \Psi(\hat{t}), \quad (27)$$

where $\chi^{\Delta\hat{t}}\circ$ denotes the operator that advances components of Ψ from their values at $\hat{t}$ through the time step $\Delta\hat{t}$. The expressions used for computing the various components of Ψ are

$$\delta_\alpha(\hat{t}+\Delta\hat{t}) = \delta_\alpha(\hat{t}) + V_{c\alpha}\Delta\hat{t},$$

$$\theta(\hat{t}+\Delta\hat{t}) = \begin{cases} \theta_{ss}(V_c) + (\theta(\hat{t}) - \theta_{ss}(V_c))e^{\left(-\frac{V_c\Delta\hat{t}}{L}\right)}, & (V_c\Delta\hat{t}/L 10^{-6}), \\ \theta(\hat{t}) + \dfrac{V_c\Delta\hat{t}}{L}(\theta_{ss}(V_c) - \theta_c), & (V_c\Delta\hat{t}/L \le 10^{-6}) \end{cases},$$

$$\Theta(l_j, \hat{t}+\Delta\hat{t}) = \frac{\Omega_c(l_j)}{\alpha_{th}\rho c l_j^2} + \left(\Theta(l_j,\hat{t}) - \frac{\Omega_c(l_j)}{\alpha_{th}\rho c l_j^2}\right)e^{\left(-\alpha_{th}l_j^2\Delta\hat{t}\right)},$$

$$\Pi(l_j, \hat{t}+\Delta\hat{t}) + \Lambda'\Theta(l_j,\hat{t}+\Delta\hat{t}) = \frac{(\Lambda+\Lambda')\Omega_c(l_j)}{\alpha_{hy}\rho c l_j^2} + \left(\Pi(l_j,\hat{t}) + \Lambda'\Theta(l_j,\hat{t}) - \frac{(\Lambda+\Lambda')\Omega_c(l_j)}{\alpha_{hy}\rho c l_j^2}\right)e^{\left(-\alpha_{hy}l_j^2\Delta\hat{t}\right)}, \quad (28)$$

where $\Omega_c(l_j)$ is obtained from equation (13) using τ_c and V_c. The dependence on the spatial indices i and k are omitted in equation (28) for compactness. Note that the integration of θ for $V_c\,\Delta\hat{t}/L > 10^{-6}$ which is based on a constant value of $V = V_c$ for $\hat{t} < t < \hat{t} + \Delta\hat{t}$, is numerically more stable during coseismic periods than the integration scheme based on a constant $\dot{\theta}$ (see Appendix B).

[25] We use two iterations to obtain second-order accurate estimates of the variables. After the first iteration, a first-order accurate predictions $\mathbf{Y}^*(t_{n+1})$ and $\Psi^*(t_{n+1})$ are obtained. After the second iteration, we correct these estimations to obtain second-order accurate estimates $\mathbf{Y}^{**}(t_{n+1})$ and $\Psi^{**}(t_{n+1})$, and adopt them as the final value at t_{n+1}.

[26] The detailed steps are as follows.

[27] 1. Obtain the first prediction $\Psi^*(t_{n+1})$ from (27)–(28) using $\mathbf{Y}_c$ and Ψ_c equal to the values at t_n throughout the time step,

$$\Psi^*(t_{n+1}) = \chi^{\Delta t}(\mathbf{Y}(t_n), \Psi(t_n)) \circ \Psi(t_n). \quad (29)$$

[28] 2. Obtain the first prediction for the functional, $\phi_\alpha^*(t_{n+1})$, by numerically integrating equation (26) assuming $\dot{D}_\beta(t') = \dot{D}_\beta(t_n)$ for $t_n < t' < t_{n+1}$ and using Fourier transform of $\delta_\alpha^*(t_{n+1})$ for $D_\alpha(t_{n+1})$.

[29] 3. Using $\phi_\alpha^*(t_{n+1})$, $\Psi^*(t_{n+1})$, equations (1) and (25), obtain the first prediction for $\mathbf{Y}(t_{n+1})$, $\mathbf{Y}^*(t_{n+1})$.

[30] 4. Make the second prediction for $\Psi(t_{n+1})$, $\Psi^{**}(t_{n+1})$, by using the first prediction for integration during the second half of the time step, Δt,

$$\Psi^{**}(t_{n+1}) = \chi^{\Delta t/2}(\mathbf{Y}^*(t_{n+1}), \Psi^*(t_{n+1})) \cdot \circ\chi^{\Delta t/2}(\mathbf{Y}(t_n), \Psi(t_n)) \circ \Psi(t_n). \quad (30)$$

Note that we can rewrite this as

$$\Psi^{**}(t_{n+1}) = \left[\chi^{\Delta t/2}(\mathbf{Y}^*(t_{n+1}), \Psi^*(t_{n+1})) \cdot \circ\chi^{-\Delta t/2}(\mathbf{Y}^{**}(t_n), \Psi^{**}(t_n))\right] \cdot \circ\chi^{\Delta t}(\mathbf{Y}(t_n), \Psi(t_n)) \circ \Psi(t_n), \quad (31)$$

showing that $[\chi^{\Delta t/2}(\mathbf{Y}^*(t_{n+1}), \Psi^*(t_{n+1})) \circ \chi^{-\Delta t/2}(\mathbf{Y}^{**}(t_n), \Psi^{**}(t_n))] \circ$ is a corrector operator. In this step, for the evolution of θ, we use a scheme based on constant V if $\max\{V(t_n), V^*(t_n)\}\ \Delta t/L > 10^{-6}$, and one based on constant $\dot{\theta}$ otherwise.

[31] 5. Repeat 2 to obtain the second prediction for the functional, $\phi_\alpha^{**}(t_{n+1})$, assuming $\dot{D}_\alpha(t') = (\dot{D}_\alpha(t_n) + \dot{D}_\alpha^*(t_{n+1}))/2$ for $t_n < t' < t_{n+1}$ where $\dot{D}_\alpha^*(t_{n+1})$ is Fourier transform of $V_\alpha^*(t_{n+1})$.

[32] 6. Repeat 3 to obtain the second prediction for $\mathbf{Y}(t_{n+1})$, $\mathbf{Y}^{**}(t_{n+1})$.

[33] 7. Adopt values with ** as the final estimate, and store $(\dot{D}_\alpha(t_n) + \dot{D}_\alpha^{**}(t_{n+1}))/2$ as the history for $t_n < t' < t_{n+1}$. Previous studies [e.g., *Lapusta et al.*, 2000; *Lapusta and Liu*, 2009] used $(\dot{D}_\alpha(t_n) + \dot{D}_\alpha^*(t_{n+1}))/2$ as the history for $t_n < t' < t_{n+1}$. We compare these two schemes in a 2-D dynamic rupture calculation on a fault governed by a linear slip-weakening law, and show that the amplitude of oscillations due to numerical error is smaller in the scheme used in this work (see Appendix D).

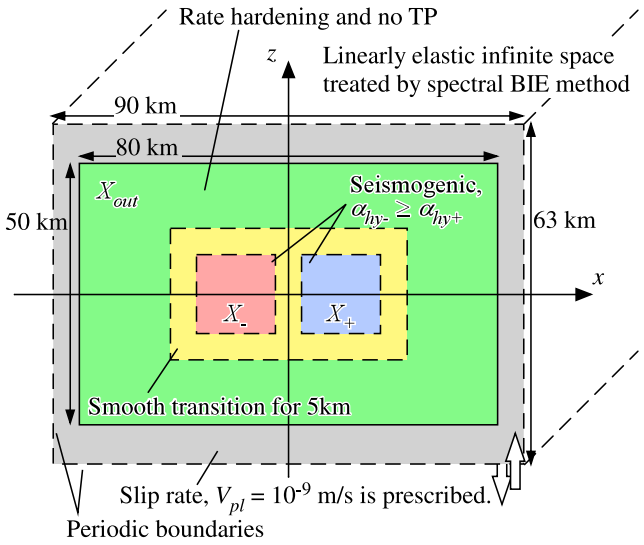

Figure 3. Schematics of the fault geometry and parameter distributions. X stands for the physical properties that may vary spatially (b, L, α_{hy}, Λ, and w). Our main goal is to explore the effect of different hydraulic diffusivity α_{hy} at the two square fault patches.

[34] Note that the integration scheme for θ is slightly different from *Lapusta and Liu* [2009] who used

$$\theta(\hat{t} + \Delta\hat{t}) = \theta(\hat{t}) + \frac{V_c \Delta\hat{t}}{L}(\theta_{ss}(V_c) - \theta(\hat{t})) \tag{32}$$

as a component of $\chi^{\Delta\hat{t}}\circ$ when $V_c\Delta t/L \leq 10^{-6}$. As shown in Appendix C, this yields a first-order accurate scheme for such slip rates, whereas the scheme used in this work is second-order accurate. We have tested both schemes in numerical simulations, and see no remarkable difference between them.

4. Application Example: Effect of Heterogeneous Hydraulic Diffusivity

4.1. Model Geometry and Physical Properties

[35] We use the developed methodology to explore the effect of heterogeneous poroelastic properties on earthquake sequences and individual seismic events. We assume a simple distribution of the poroelastic properties that creates two patches of different hydraulic diffusivity and hence different effectiveness of the shear-heating induced thermal pressurization (TP). Our study is motivated by observations of heterogeneous hydraulic properties of natural faults. Hydraulic properties on faults vary depending on the depth [*Faulkner*, 2004], local geology, the type of host rocks, and the deformation history. *Tanikawa and Shimamoto* [2009] measured hydraulic properties of fault rocks collected at boreholes by the Chelungpu fault, Taiwan, a source fault of the 1999 Chi-Chi earthquake, at about 200 m and 300 m below the surface in the northern and southern regions, respectively. They concluded that the south has higher permeability (larger α_{hy}) than the north by several orders of magnitude.

[36] The geometry of the simulated fault and the assumed distributions of physical properties are illustrated in Figure 3. The physical parameters used in this study are listed in Table 1. We consider a potentially seismogenic fault region with velocity-weakening steady state friction surrounded with a velocity-strengthening region. Outside the velocity-strengthening region, steady slow slip with slip velocity $V_{pl} = 10^{-9}$ m/s is prescribed in the z direction. The overall fault segment, with dimensions of 90 km and 63 km in the x and z directions, respectively, is periodically repeated to produce an infinite fault plane. Note that the spectral BIEM using a Fourier basis requires periodic boundary conditions along the fault, and hence we cannot rigorously introduce the effect of a free surface. The seismogenic fault segment contains two square patches, 15 km × 15 km each, with uniform physical properties within each patch (Figure 3). In this study, only hydraulic diffusivity α_{hy} may be different for the two patches. Between the seismogenic patches and the surrounding velocity-strengthening region, there is a smooth transition zone in which properties that differ in the patches and/or in the surrounding velocity-strengthening region vary according to a smoothed boxcar function:

$$\begin{aligned} X(x,z,t) = X_{out} &+ (X_+ - X_{out})B(x-10;7.5,12.5)B(z;7.5,12.5) \\ &+ (X_- - X_{out})B(x+10;7.5,12.5)B(z;7.5,12.5), \end{aligned} \tag{33}$$

where X stands for the fault property that varies with space, the numbers are in km, and

$$B(x;W_1,W_2) = \begin{cases} 1, & |x| < W_1; \\ 0, & W_2 < |x|; \\ \frac{1}{2} - \frac{1}{2}\tanh\left(\frac{W_2}{|x|-W_1-W_2} + \frac{W_2}{|x|-W_1}\right) & \text{otherwise.} \end{cases} \tag{34}$$

Note that if the two patches have the same value of a physical property, then that physical property is uniform in the region

Table 1. Physical Properties and Model Parameters

	Symbol	Value
Elastic Properties		
Shear modulus	μ	30 GPa
Poisson's ratio	ν	0.25
Shear wave speed	c_s	3 km/s
Frictional Properties		
Reference slip rate	V_0	1 μm/s
Steady state friction at V_0	f_0	0.6
State evolution distance	L_{out}	1000 mm
	$L_+ = L_-$	4 mm
Direct effect parameter	a	0.01
Evolution effect parameter	b_{out}	0
	$b_+ = b_-$	0.014
Hydrothermal Properties		
Specific heat	ρc	2.7 MPa/K
Thermal diffusivity	α_{th}	10^{-6} m^2/s
Hydraulic diffusivity	α_{hyout}	10^{-2} m^2/s
	α_{hy+}	10^{-2}–10^{-5} m^2/s
	α_{hy-}	10^{-2}, 10^{-4} m^2/s
Undrained $\Delta p/\Delta T$	Λ_{out}	0
	$\Lambda_+ = \Lambda_-$	0.1 MPa/K
Half width of shear zone	w_{out}	1000 mm
	$w_+ = w_-$	10 mm, 5 mm
Initial and Boundary Conditions		
Effective normal stress	σ_{e0}	30 MPa
Loading rate	V_{pl}	10^{-9} m/s

$-17.5\ \text{km} < x < 17.5\ \text{km}$ and $-7.5\ \text{km} < z < 7.5\ \text{km}$ that includes both patches and the transition zone between them.

[37] We assume elastodynamic and rate-and-state friction properties similar to those given by *Lapusta and Liu* [2009] and previous studies. The elastodynamic (bulk) properties are as follows: shear modulus $\mu = 30$ GPa, Poisson's ratio $\nu = 0.25$, and S wave speed $c_s = 3$ km/s. Rate and state parameters f_0, V_0, and a are uniform over the entire fault and equal to 0.6, 1 μm/s, and 0.01, respectively. Rate and state parameter b varies so that $b = b_{out} = 0$ in the velocity-strengthening region and $b_- = b_+ = 0.014$ in and between the velocity-weakening patches. The characteristic slip L is uniform in the patches at 4 mm and increases to 1 m in the velocity-strengthening region in order to arrest ruptures there more efficiently. The initial effective normal stress σ_e is set at 30 MPa. Such relatively low σ_e contributes to keeping shear zone temperatures below the melting point, as discussed further in section 4.4.2. Note that we are not suggesting that uniform distribution of σ_e is characteristic of the active faults. In general, the effective effective normal stress tends to increase with depth. We adopted this assumption because it is simple and may be applicable to active faults in regions where high excess pore pressure is expected to exist at depth (e.g., sedimentary basins, oil fields, and subduction zones) [e.g., *Suppe and Wittke*, 1977; *Rice*, 1992; *Tanikawa et al.*, 2008].

[38] For thermal properties, we use the thermal diffusivity $\alpha_{th} = 1.0 \times 10^{-6}$ m^2/s and the specific heat capacity $\rho c = 2.7$ MPa/K, which are representative of the values obtained in various studies. Thermal transport properties depend on the rock type and condition. *Rempel and Rice* [2006] and *Rice* [2006] estimated $\alpha_{th} = 0.5$–0.7×10^{-6} m^2/s and $\rho c = 2.7$ MPa/K for the Median Techtonic Line (MTL), southwest Japan, at the ambient conditions at 7 km (126 MPa effective confining pressure and 210°C). *Kano et al.* [2006] and *Tanaka et al.* [2006] quantitatively discussed the heat transport process from the fault plane based on observations at boreholes in the northern region of the Chelungpu fault. *Kano et al.* [2006] used $\alpha_{th} = 0.34 \times 10^{-6}$ m^2/s and $\rho c = 3.74$ MPa/K to explain the measured temperature anomaly around the fault plane at a borehole by TCDP (Taiwan Chelungpu Drilling Project) at 1110 m below the ground surface. *Tanaka et al.* [2006] explained the temperature anomaly observed at a shallow borehole (at 300–330 m depth) using laboratory-measured thermal transport properties of samples collected there. They reported $\alpha_{th} = 1.47 \times 10^{-6}$ m^2/s and $\rho c = 0.73$ MPa/K.

[39] Hydraulic transport properties vary by orders of magnitude, which motivates our study of a fault with variable hydraulic properties. *Rempel and Rice* [2006] and *Rice* [2006] estimated $\Lambda = 0.34$–0.98 MPa/K and $ha_{hy} = 0.86$–3.52×10^{-6} m^2/s for the hydraulic transport properties on MTL, at the ambient conditions at 7 km, based on the study by *Wibberley and Shimamoto* [2003]. The MTL is one of the most mature faults in Japan; it has slipped 100–200 km since mid-Cretaceous [e.g., *Takagi and Shibata*, 2000]. Studies on the permeability structure around the fault core of less mature faults show higher permeability by orders of magnitude [e.g., *Tsutsumi et al.*, 2004; *Noda and Shimamoto*, 2005]. Using the laboratory measurements by *Tanikawa and Shimamoto* [2009] for porosity and permeability of the fault rocks from the Chelungpu fault at 30 MPa effective pressure, and assuming water thermal expansivity of 5×10^{-4} and water viscosity of 2×10^{-4} Pas, we can estimate $\Lambda = 2.4$–7×10^{-2} MPa/K (north), 4.1–5.1 $\times 10^{-2}$ MPa/K (south), and $\alpha_{hy} = 7.2$–7.5×10^{-5} (north), 2.7×10^{-2} to 7.3×10^{-4} (south). In our study, we choose $\Lambda_+ = \Lambda_- = 0.1$ MPa/K, $\alpha_{hy-} = 10^{-2}$ or 10^{-4} m^2/s, and $\alpha_{hy+} = 10^{-5}$–10^{-2} m^2/s, which are within the range of the reported values for seismogenic regions. In the velocity-strengthening region, we assign values $\Lambda_{out} = 0$ and $\alpha_{hyout} = 10^{-2}$ m^2/s which disable thermal pressurization there. *Rice* [2006] determined the characteristic slip L_* required for TP in the case of slip on a mathematical plane,

$$L_* = \frac{4}{f^2}\left(\frac{\rho c}{\Lambda}\right)^2 \frac{\left(\sqrt{\alpha_{th}} + \sqrt{\alpha_{hy}}\right)^2}{V}. \tag{35}$$

With $f = 0.6$, $\rho c = 2.7$ MPa/K, $\Lambda = 0.1$ MPa/K, $\alpha_{th} = 1 \times 10^{-6}$ m^2/s, and $V = 1$ m/s, the hydraulic diffusivity of $\alpha_{hy} = 1 \times 10^{-2}$ m^2/s results in $L_* = 81$ m which is much larger than total slip in one coseismic event. Thus, TP is not efficient if $\alpha_{hy} = 10^{-2}$ m^2/s is assumed. For $\alpha_{hy} = 1 \times 10^{-4}$ m^2/s, the characteristic slip reduces to 0.8 m, which makes TP and the associated dynamic weakening quite pronounced during seismic slip.

[40] In most of the study, we use $w = 10$ mm for the width of the shearing zone; this parameter determines the shape of the heat source in equation (4). Similar values have been assumed in several previous studies based on field data [*Tanikawa and Shimamoto*, 2009]. However, smaller values for the width of the actively shearing zones have also been reported and may be more realistic. The localization of shear deformation in zones of submillimeter thickness have been observed at exhumed faults and in drill cores [*Chester and Chester*, 1998; *Chester et al.*, 2004; *Heermance et al.*, 2003; *Mizoguchi and Shimamoto*, 2004] as well as in specimens after rotary shear experiments [*Beeler et al.*, 1996; *Mizoguchi and Shimamoto*, 2004]. Further studies are needed to give better constraints or a model for w which may evolve throughout the earthquake cycle. Note that submillimeter shear zones cause very rapid weakening at the rupture front that is difficult to resolve numerically. This limits simulations with thin shear zones to cases of single dynamic ruptures in 2-D models with faults that are of the order of a ten meters [*Noda et al.*, 2009]. Hence we use $w = 10$ mm for the problem to be numerically tractable. In addition, narrower slip zones lead to temperatures high enough to cause melting, as we demonstrate in section 4.4.2 for $w = 5$ mm. Since melting is not included in our constitutive description, such calculations would be no longer physically self-consistent, as discussed in section 4.4.2. Incorporation of rock melting and other chemical reactions into fault constitutive laws is an important future step to further investigate the geologically realistic earthquake generation process.

[41] The initial conditions, at $t = 0$, are assigned assuming that the fault is in steady state sliding, with V_z equal to the

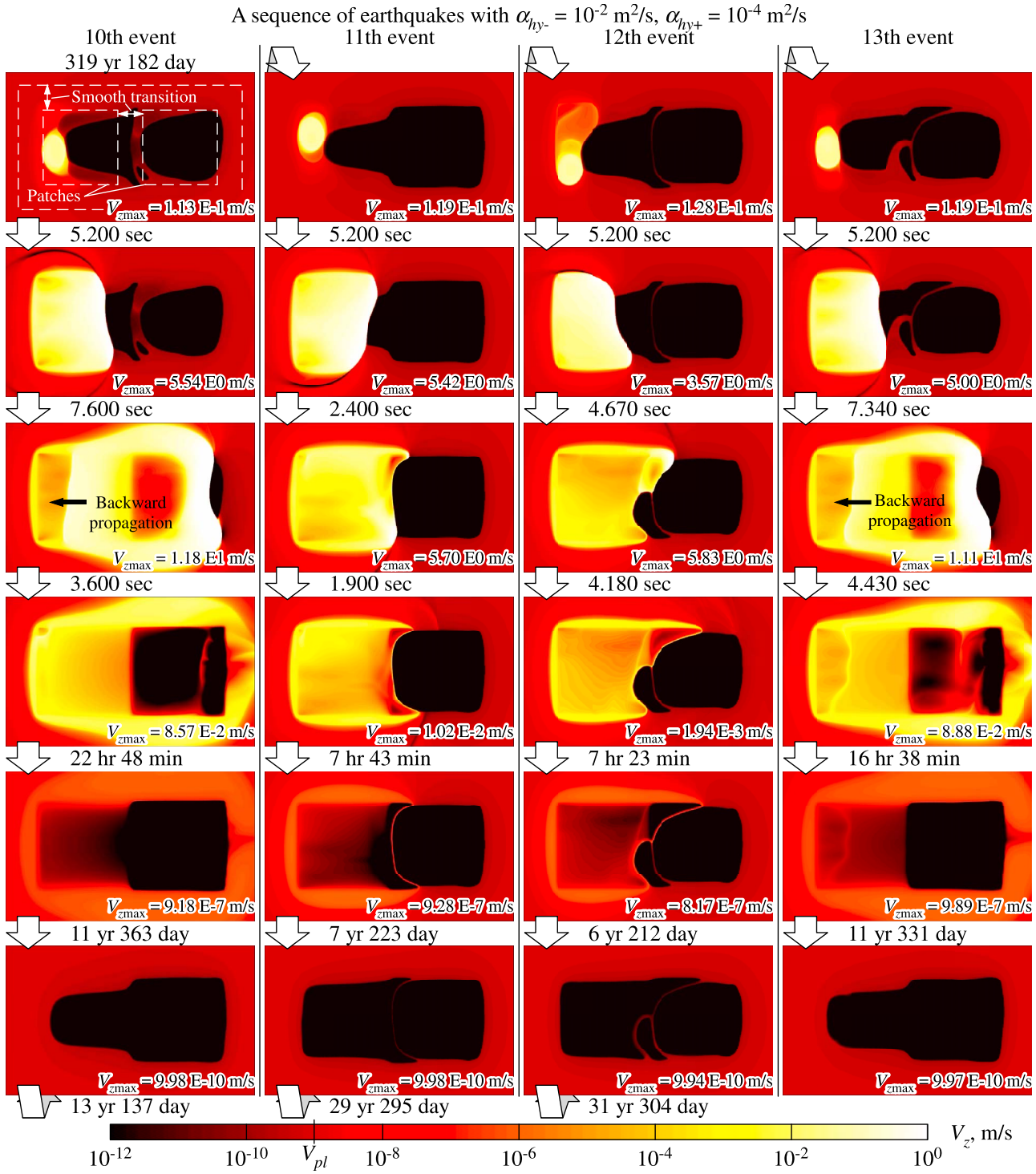

Figure 4. Snapshots of slip rate distribution for a sequence of earthquakes in the case with α_{hy-} = 10^{-2} m^2/s, and α_{hy+} = 10^{-4} m^2/s. (first and fourth columns) Model-spanning events are associated with a backward rupture propagation as indicated by arrows. (second and third columns) Smaller events preferably extend along the boundary between creeping and locked regions.

loading rate of $V_{pl} = 10^{-9}$ m/s and $V_x = 0$. This determines the corresponding initial values of the state variable θ and the shear stress τ_z, with $\tau_x = 0$. Since T and p measure changes from the initial values, their values at $t = 0$ are zero. At $t = 0+$, a Gaussian-shaped perturbation is added to τ_{0z} with the amplitude of 3 MPa and the standard deviation of $1/\sqrt{2}$ km. The perturbation is centered at $x = -10$ km and $z = -5$ km unless otherwise noted. The long-term behavior of the model is unaffected by the location of the initial perturbation, as discussed in section 4.5.

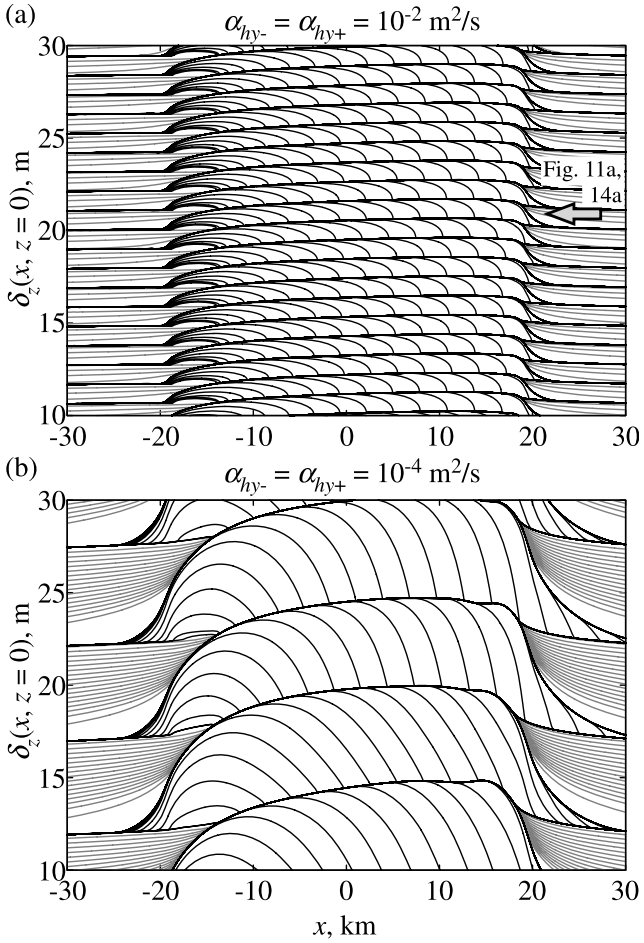

Figure 5. Earthquake sequences in the cases with uniform hydraulic diffusivity of (a) $\alpha_{hy-} = \alpha_{hy+} = 10^{-2}$ m^2/s and (b) 10^{-4} m^2/s. Slip accumulation at the middepth of the fault, $z = 0$, is shown, with gray lines plotted every 10 years and black lines plotted every 1 s for coseismic periods. All events span the entire seismogenic region, and more efficient TP produces larger coseismic slip.

4.2. Numerical Parameters

[42] *Lapusta and Liu* [2009] discussed the following criterion for spatial discretization in terms of the resolution of the cohesive zone at the rupture front. A rate- and state-dependent friction law in the aging formulation yields the slip-weakening rate W_{RS} at the rupture front given by

$$W_{RS} = \frac{b\sigma_e}{L}. \tag{36}$$

The cohesive zone size R_0 at the rupture speed $c \to 0^+$ is

$$R_0 = \frac{9\pi}{32}\frac{\mu^*}{W} = \frac{9\pi}{32}\frac{\mu^* L}{b\sigma_e}, \tag{37}$$

where μ^* is equal to μ for mode III and $\mu/(1 - \nu)$ for mode II. R_0 has to be discretized by at least three to five grid points for adequate numerical resolution [*Day et al.*, 2005]. With our selection of the physical properties, we have $W_{RS} \le 105$ MPa/m which leads to $R_0 \ge 252$ m. We choose the spatial grid interval to be $h = 60$ m so that $R_0/h \ge 4.2$. We have tested calculations with $h = 100$ m and found that the main features of the earthquake sequences discussed in the following sections do not change. Note that TP may affect the needed resolution by enhancing the weakening rate. Under the adiabatic and undrained conditions which give the upper bound to the rate of pore pressure rise, the weakening rate due to TP is given by

$$W_{TP} = \frac{f\tau\Lambda}{\sqrt{2\pi}w\rho c}, \tag{38}$$

which is 28 MPa/m with $f = 0.8$ and $\tau = 24$ MPa which are the estimate of the values at the rupture front. Therefore, TP only modestly affects the numerical resolution in the cases considered in this study. If we use a much thinner shear zone or a larger value of Λ, the resolution of weakening due to TP would control the spatial grid size.

[43] We adopt the same time step controller as used by *Lapusta et al.* [2000] and *Lapusta and Liu* [2009]:

$$\Delta t = \max\{\Delta t_{\min}, \Delta t_{evol}\}, \tag{39}$$

where

$$\Delta t_{\min} = h/3c_s \tag{40}$$

and

$$\Delta t_{evol} = \min_{i,k}[\xi(x_i, z_k, t)L(x_i, z_k)/V(x_i, z_k, t), L(x_i, z_k)/3V(x_i, z_k, t)], \tag{41}$$

with $L(x_i, z_k)$, $\xi(x_i, z_k, t)$, and $V(x_i, z_k, t)$ being the characteristic slip, the friction-dependent coefficient, and the slip rate for the cell (i, k), $i = 1,2, \ldots, N_x$ and k = 1,2, …, N_z, respectively. Coefficients $\xi(x_i, z_k, t)$ depend on friction properties and are obtained from stability analyses given in Appendix B. Note that the choice of the friction parameters for the seismogenic region yields $\xi = 0.63$ for $\sigma_e = 30$ MPa. Hence the coefficient 1/3 in (41) is more restrictive unless ξ is decreased by pore pressurization. The stepping scheme (39)–(41) results in time steps that range from $\Delta t_{\min} = 1/150$ s to $\Delta t = 3.82 \times 10^5$ s in the simulations we have done.

[44] The discretization used in computing the evolution of temperature and pore pressure is explained in section 2.3 and Appendix A.

4.3. Complexity of Long-Term Fault Slip

4.3.1. Long-Term Slip Accumulation and Magnitude-Time Sequence

[45] The developed methodology allows us to simulate all stages of the earthquake cycle, from the interseismic slip, to the accelerating slip in the nucleation zone, to the subsequent dynamic rupture, and to the following postseismic slip. As an example, consider the simulation with $\alpha_{hy-} = 10^{-2}$ m^2/s and $\alpha_{hy+} = 10^{-4}$ m^2/s. Figure 4 illustrates the evolution of slip rate in the time period that includes four seismic events, starting with the tenth simulated event. The panels show snapshots of slip velocity distribution on the fault, on the logarithmic scale. White and light yellow colors correspond to coseismic slip rates, darker yellow and orange point to aseismic slip faster than the plate rate, red corre-

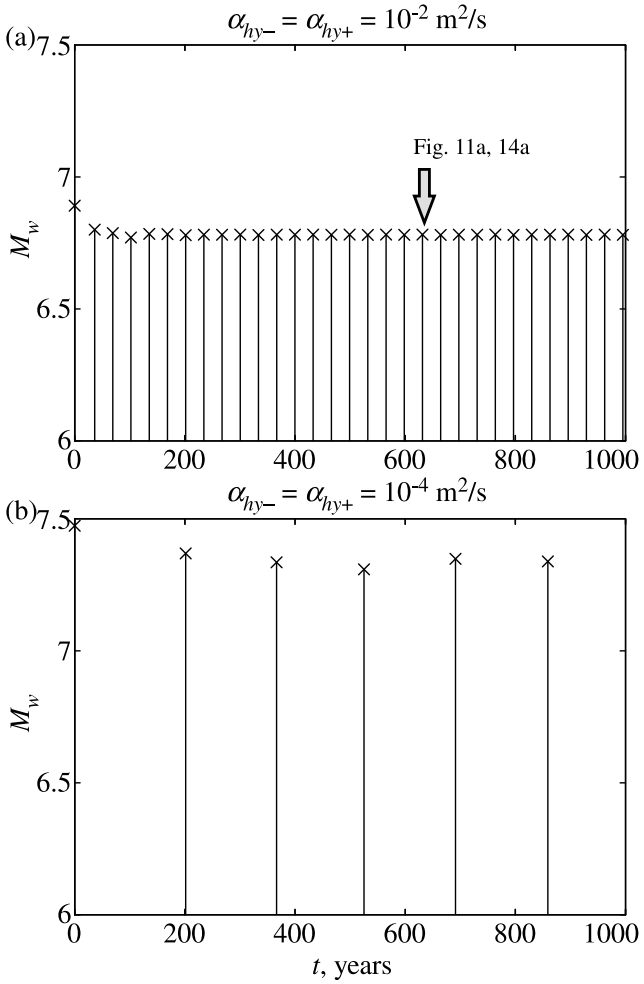

Figure 6. Moment magnitude of the earthquakes obtained in the simulations shown in Figure 5 for (a) $\alpha_{hy-} = \alpha_{hy+} = 10^{-2}$ m^2/s and (b) $\alpha_{hy-} = \alpha_{hy+} = 10^{-4}$ m^2/s. In both cases, characteristic events of the same size occur regularly.

sponds to slip rates close to the plate rate, and near-black indicates locked portions of the fault. The numbers between the panels give the interpanel time. Figure 4 (first three panels of first column) illustrates the tenth event in the simulation. The event starts at the left side of the seismogenic region and propagates toward the right with the rupture speeds in the range of 1–2 km/s. Figure 4 (fourth and fifth panels) show immediate postseismic slip (right after and about 10 h after the event, respectively). The interseismic state of the fault, with the black locked region, is shown in Figure 4 (bottom row, first column). Note that the tenth event ruptures the entire seismogenic part of the fault. In the following, we are going to call such events "model spanning." Figure 4 (second and third columns) illustrates the following two earthquake cycles, both of which contain a smaller seismic event that fully ruptures only the left patch. Figure 4 (fourth column) shows the thirteenth event which again ruptures the entire seismogenic region. More detailed results from this simulation are discussed in the following.

[46] To explore the effect of heterogeneous hydraulic properties on the long-term fault behavior, we start with the cases of homogeneous hydraulic properties $\alpha_{hy-} = \alpha_{hy+}$ (Figures 5 and 6) for comparison. Figure 5 shows snapshots of slip distribution along the middepth of the fault ($z = 0$) every 10 years (gray lines) and every 1 s coseismically (black lines). Figure 6 gives the moment magnitude of the

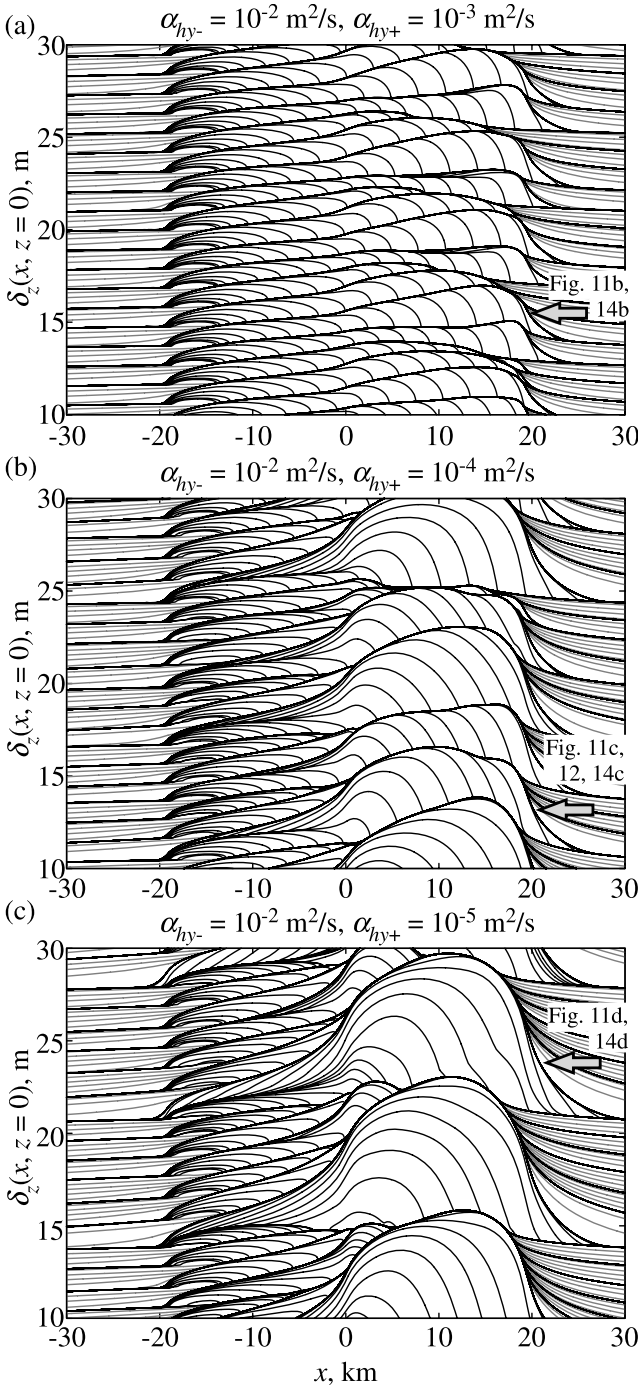

Figure 7. Effect of spatial variation in hydraulic diffusivity on earthquake sequences in the cases with $\alpha_{hy-} = 10^{-2}$ m^2/s and (a) $\alpha_{hy+} = 10^{-3}$, (b) 10^{-4}, and (c) 10^{-5} m^2/s. The meaning of the lines is the same as in Figure 5. As the heterogeneity in α_{hy} becomes stronger, the pattern of slip accumulation becomes more complex with one cycle having multiple events of different sizes.

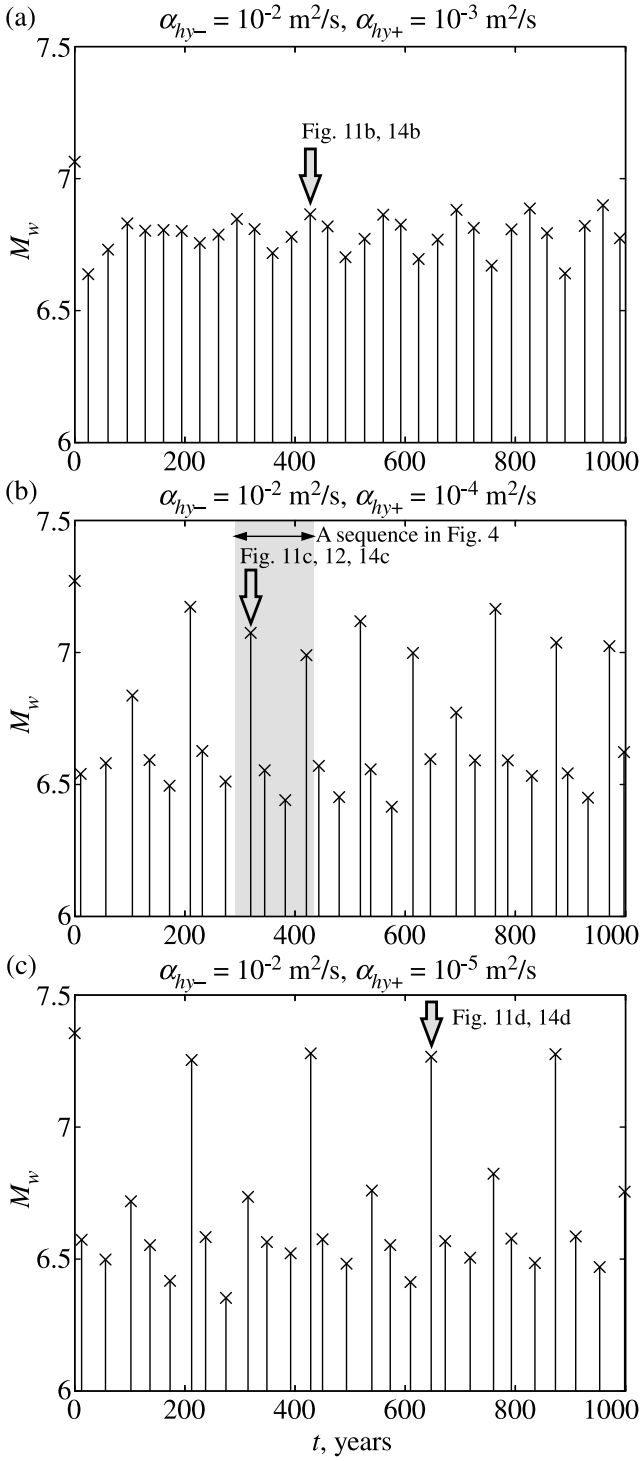

Figure 8. Moment magnitude of the earthquakes obtained in the simulations shown in Figure 7, with $\alpha_{hy-} = 10^{-2}$ m^2/s and (a) $\alpha_{hy+} = 10^{-3}$, (b) 10^{-4}, and (c) 10^{-5} m^2/s. Increasing heterogeneity in α_{hy} produces a longer period between model-spanning events, with several smaller events in between.

seismic events, M_w, as a function of time. The beginning of dynamic rupture is defined as the time when the maximum slip rate exceeds 0.1 m/s [*Bizzarri and Belardinelli*, 2008]. The end of dynamic rupture is defined as the time when the slip rate drops below 0.1 m/s and does not increase back to the values above 0.1 m/s in the time equal to the elastodynamic time window t_w. We see that if α_{hy} is uniform in the seismogenic zone, earthquake sequences are simple, with only one characteristic model-spanning event (Figures 5 and 6). The case with uniformly more efficient TP (Figures 5b and 6b) produces larger events and thus a longer recurrence interval.

[47] For cases with different α_{hy} in the two patches, the behavior is more complex. When the difference is large enough, the patch with more efficient TP produces larger slip during a model-spanning event similarly to what is observed in the 1999 Chi-Chi earthquake, Taiwan [e.g., *Ma et al.*, 2003], and thus the patch does not rupture in every event (Figures 7b and 7c). Note that *Manighetti et al.* [2005] reported that the hypocenter and the maximum slip typically occur at different locations in natural earthquakes. The slip deficit in the other patch is filled with several smaller events. For less significant difference in α_{hy} (i.e., $\alpha_{hy-} = 10^{-2}$ m^2/s, $\alpha_{hy+} = 10^{-3}$ m^2/s), most of the events are model-spanning but there is a variation in M_w (Figures 7a and 8a). Hence

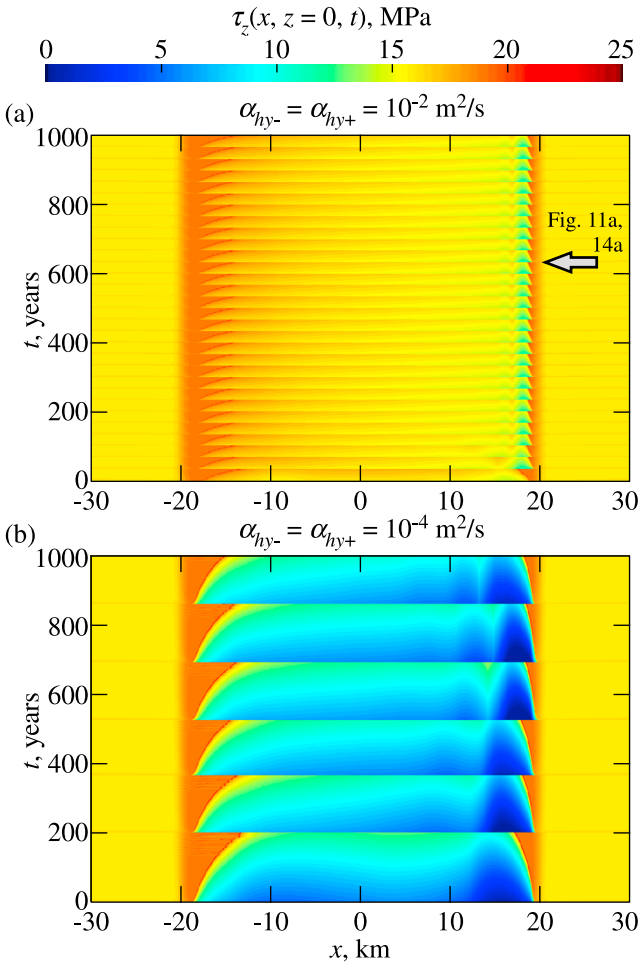

Figure 9. Distribution of shear stress $\tau_z(x, z = 0, t)$ along the middepth of the fault plotted every year for the cases of Figure 5, with (a) $\alpha_{hy-} = \alpha_{hy+} = 10^{-2}$ m^2/s and (b) 10^{-4} m^2/s. More efficient TP results in lower intersesmic shear stress.

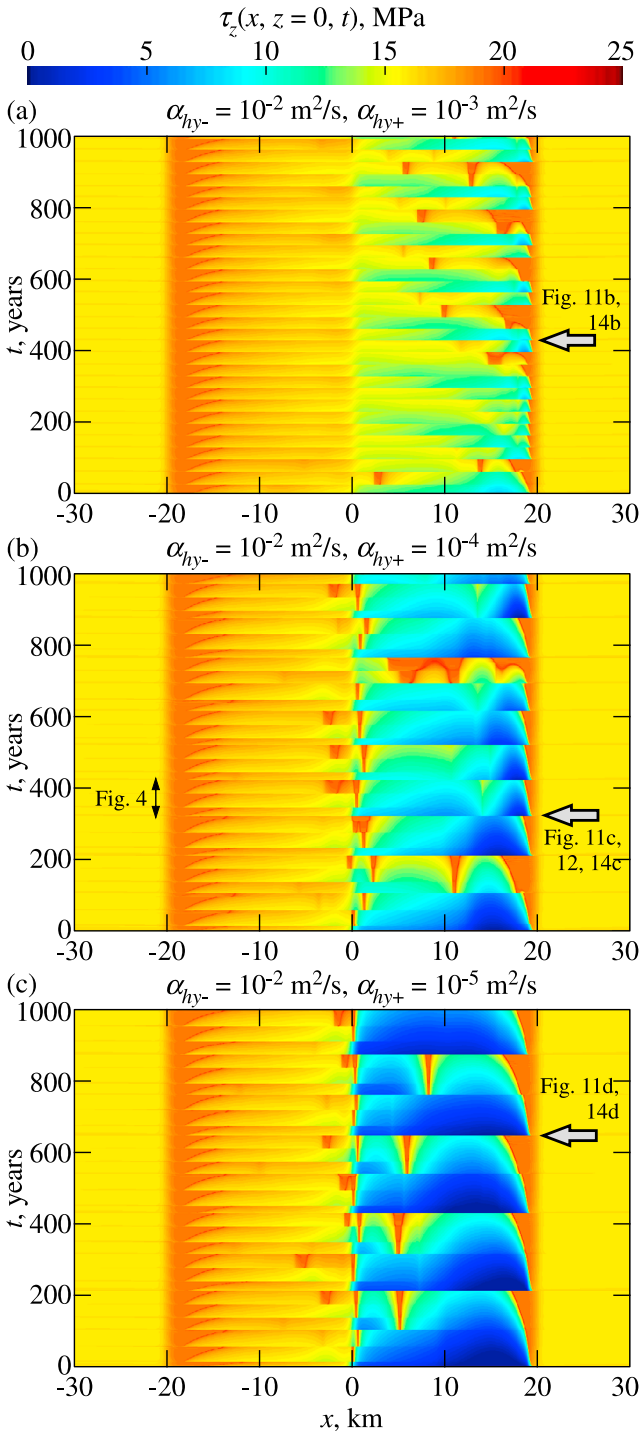

Figure 10. Distribution of shear stress $\tau_z(x, z = 0, t)$ along the middepth of the fault plotted every year for the cases of Figure 7, with $\alpha_{hy-} = 10^{-2}$ m^2/s and (a) $\alpha_{hy+} = 10^{-3}$, (b) 10^{-4}, and (c) 10^{-5} m^2/s. Locally efficient TP lowers intersesmic shear stress there. For the case of the strongest heterogeneity in α_{hy}, (Figure 10c), the interseismic shear stress in the less permeable region is as low as 5 MPa, which is several times lower than static friction, by which we mean the low-velocity friction resistance of the fault.

heterogeneity in α_{hy} results in more complex earthquake sequences, with supercycles that contain events of variable sizes (Figure 8).

4.3.2. Heterogeneity in the Interseismic Shear Stress

[48] Our simulations show that regions with lower hydraulic diffusivity, and hence more efficient TP, have lower interseismic shear stress. Figures 9 and 10 show time histories of the dominant shear stress component, τ_z, at $z = 0$ for the cases with $\alpha_{hy-} = \alpha_{hy+}$ and $\alpha_{hy-} > \alpha_{hy+}$, respectively. If the seismogenic region were steadily sliding at V_{pl}, the shear stress there would be 17.2 MPa. This can be taken as a measure of static friction, corresponding to the friction coefficient of 0.57. In regions where TP is not efficient ($\alpha_{hy} = 10^{-2}$ m^2/s), τ_z differs from that value only modestly (Figure 9a and the region given by -17.5 km $< x < -2.5$ km in Figures 10a, 10b, and 10c). For smaller α_{hy}, the corresponding regions experience larger slip and stress drop, and the interseismic shear stress decreases (Figure 9b; the region given by 2.5 km $< x <$ 17.5 km in Figures 10a, 10b, and 10c), to values as low as 5 MPa or the equivalent friction coefficient of 0.17. For sufficiently low hydraulic diffusivities, the decrease is large enough to stop several ruptures propagating from the left patch of higher hydraulic diffusivity. After such smaller events arrest, stress concentrations are left ahead of the arrested rupture front (red vertical streaks in the region given by 2.5 km $< x <$ 17.5 km in Figures 10a, 10b, and 10c), which persist throughout the interseismic period.

[49] Previous studies [e.g., *Bizzarri and Cocco*, 2006b] showed that more efficient thermal pressurization causes larger slip and thus larger stress drop, by conducting simulations of dynamic rupture propagation with prescribed initial conditions on the fault. We would like to emphasize that our study is substantially different. In simulations of a sequence of earthquakes, as we conduct here, the initial conditions for each dynamic event are determined by the simulation itself based on prior behavior of the model. We are investigating the entire source process for the sequence of earthquakes, and the effect of thermal pressurization is discussed in that context.

[50] Note that the distribution of shear stress before a typical dynamic event (aside from several initial events) is quite different from what is often assumed (e.g., steady state sliding or uniform background shear stress) in single-rupture calculations with heterogeneous fault properties. This point highlights the importance of studying the effect of fault heterogeneity in the context of earthquake sequences.

[51] In our model, the shear stress in the patch of lower α_{hy} remains lower even before events that span the entire seismogenic region, because of its ability to sustain rupture propagation at low prestress. Previous studies [*Perrin et al.*, 1995; *Zheng and Rice*, 1998; *Lapusta and Rice*, 2003; *Noda et al.*, 2009; *Rice et al.*, 2009] also focused on propagation of ruptures at low shear prestress compared to the static strength of rocks in the laboratory. Such low shear prestress can be inferred for natural faults, for example, from the measurements of the principal stress directions at boreholes around the San Andreas fault [*Hickman and Zoback*, 2004; *Townend and Zoback*, 2004]. Our simulations show that dynamic fault weakening indeed determines the level of long-term shear stress acting on a fault.

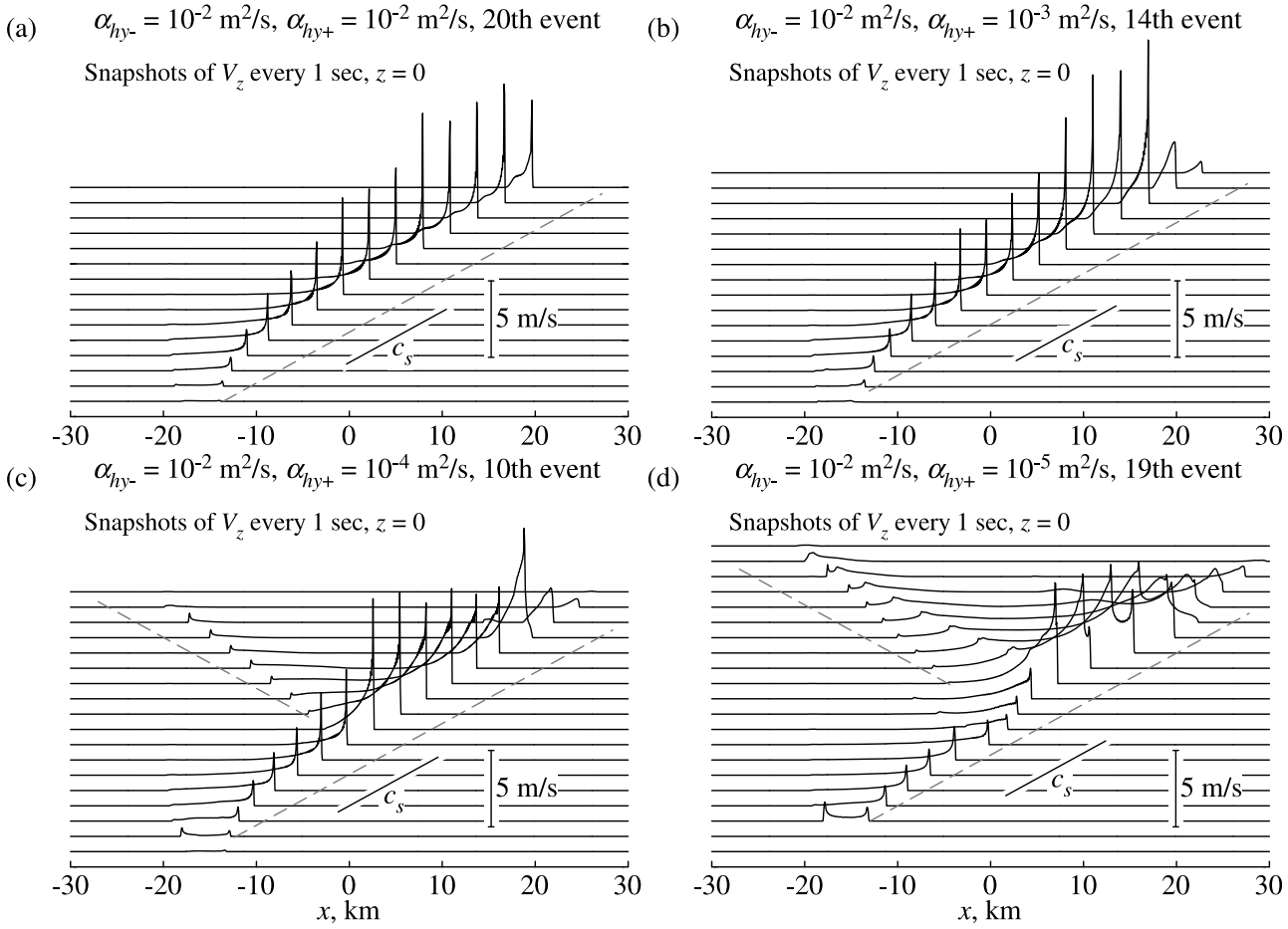

Figure 11. Snapshots of slip rate distribution, $V_z(x, z = 0)$, in typical model-spanning events, plotted every 1 s, for cases with $\alpha_{hy-} = 10^{-2}$ m^2/s and (a) $\alpha_{hy+} = 10^{-2}$, (b) 10^{-3}, (c) 10^{-4}, and (d) 10^{-5} m^2/s. The events shown are marked in Figures 5–10. More efficient TP increases the final slip not by increasing the maximum slip rate but by widening the slip pulse and causing backward rupture propagation (Figures 11c and 11d). Also see Figure 4.

4.4. Complexity of Individual Earthquakes

4.4.1. Characteristics of Model-Spanning Events

[52] By conducting earthquake sequence calculations that resolve all inertial effects during each seismic event, we can study not only long-term fault behavior but also characteristics of individual dynamic events consistent with long-term history of fault slip.

[53] To visualize propagation of typical model-spanning events, we plot (Figure 11) the corresponding snapshots of coseismic slip rate distribution along the middepth of the fault for the events indicated by arrows in Figures 5, 6, 7, 8, 9, and 10. The evolution of slip rate becomes more complex for cases with larger heterogeneity in hydraulic diffusivity. In particular, we observe broadening of the area of active slip in the right patch for cases with more efficient TP there. This can be attributed to the backward rupture propagation from the right patch to the left patch, after ruptures start to achieve much larger slip in the right patch. Figure 11c shows the backward rupture front in the event shown in Figure 4 (first column) (the tenth event with $\alpha_{hy-} = 10^{-2}$ m^2/s and $\alpha_{hy+} = 10^{-4}$ m^2/s). The propagation is driven by the stress concentration around the high-slip region. While the

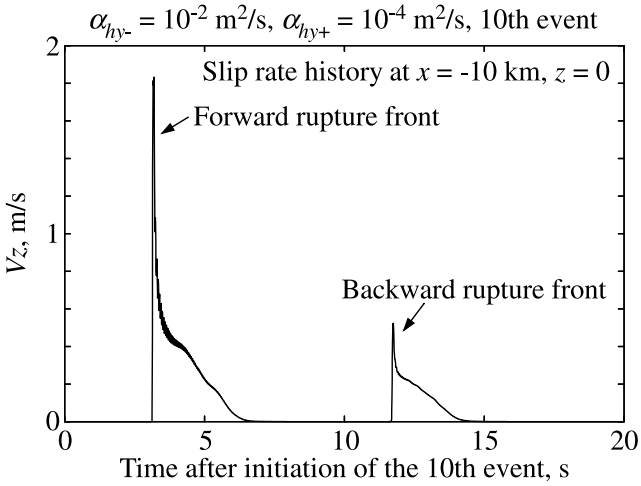

Figure 12. The source time function at a location ($x = -10$ km and $z = 0$) that experiences both forward and backward rupture fronts during this event. The amount of slip due to the backward rupture is a significant fraction of the total slip during this event.

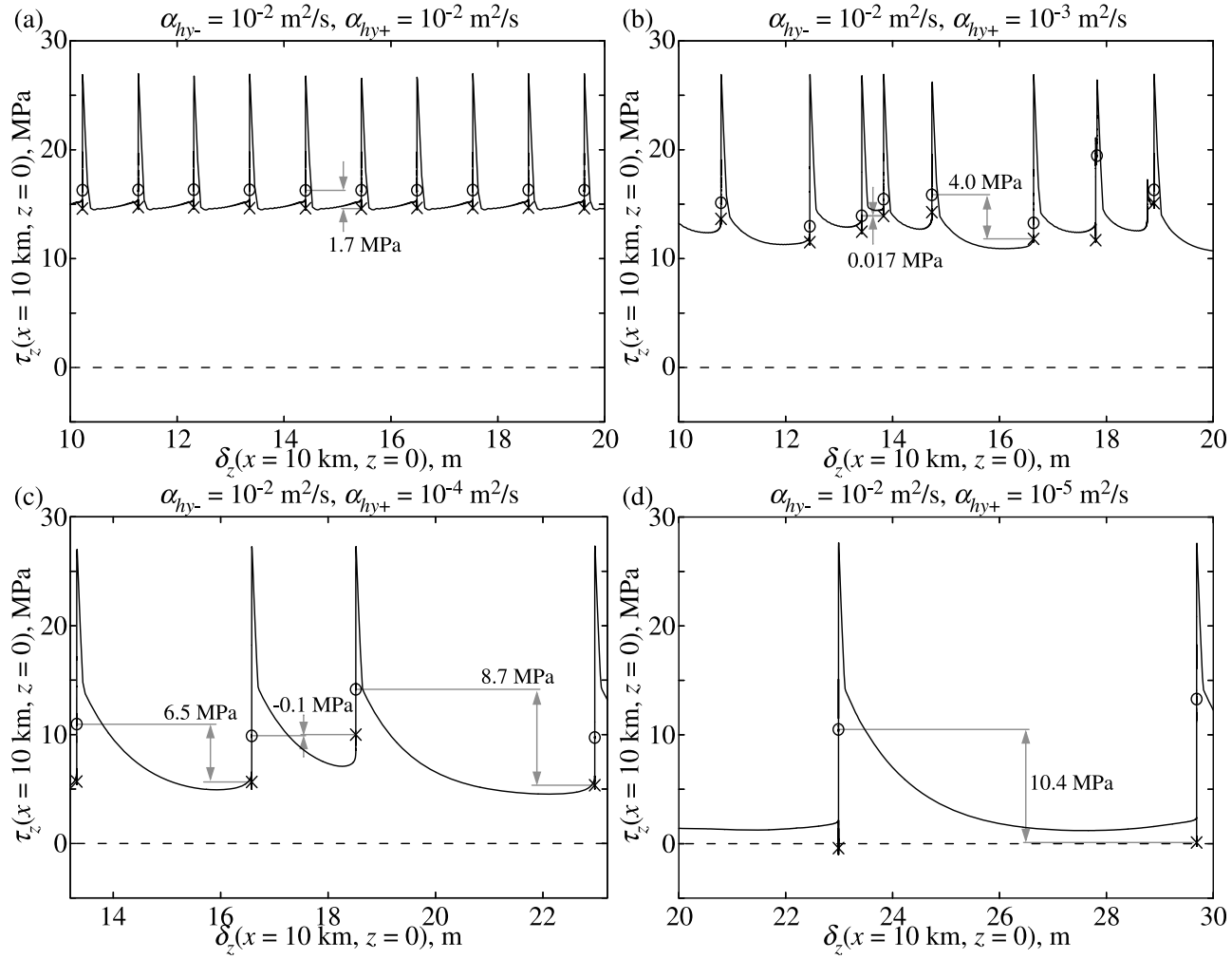

Figure 13. Shear stress τ_z as a function of slip δ_z at the fault location given by $x = 10$ km and $z = 0$, for the cases with $\alpha_{hy-} = 10^{-2}$ m^2/s and (a) $\alpha_{hy+} = 10^{-2}$, (b) 10^{-3}, (c) 10^{-4}, and (d) 10^{-5} m^2/s. Circles and crosses mark the initiation and termination of model-spanning events. More efficient TP produces larger slip and a longer apparent slip-weakening distance, as pointed out by *Rice* [2006].

peak slip rate at this backward rupture front is much smaller than the one for the forward rupture front (Figure 12), the additional slip due to this backward propagation can be a significant fraction of the total slip in some areas of the fault (Figures 7c and 12). If such features occur in natural events, then seismic inversions would need to assume quite a general source time function (Figure 12) to accurately capture the event kinematics.

[54] As shown in Figure 11, rupture speed varies locally because of the heterogeneous prestress and the resulting complex rupture process (see Figures 10c and 11d). Note that Figure 11 shows rupture behavior along a section at $z = 0$. As a result, the local rupture speed may appear to exceed c_s if rupture propagates obliquely to the middepth plane. This occurs, for example, in two locations in the case plotted in Figure 11d: near the nucleation, which is off the middepth plane, and between $x = 10$ and 20 km.

[55] It is interesting to point out that the larger final slip does not necessarily corresponds to the larger maximum slip rate, when different events are compared. If we compare slip rates in the region $0 < x < 20$ km for the events shown in Figure 11, the case of Figure 11d has the smallest peak slip rates there but the largest final slip (Figures 5 and 7).

[56] As discussed in section 4.2, the rate-and-state weakening (i.e., the evolution of the state variable θ) is the dominant weakening mechanism at the rupture front in the cases presented in this study. Figure 13 represents τ_z as a function of δ_z at $x = 10$ km, with circles and crosses indicating initiations and terminations of dynamic events. A sharper drop in τ_z at the rupture front due to rate-and-state weakening is followed by the more gradual weakening due to TP, if the latter is efficient. More efficient TP produces more significant dynamic weakening as well as larger slip [e.g., *Andrews*, 2002; *Bizzarri and Cocco*, 2006b; *Noda et al.*, 2009].

[57] Note that, in the seismogenic region, most of the slip and thus heat is generated coseismically. The area below the curves in Figure 13 represents the local heat generation, which is clearly smaller for cases with more efficient TP.

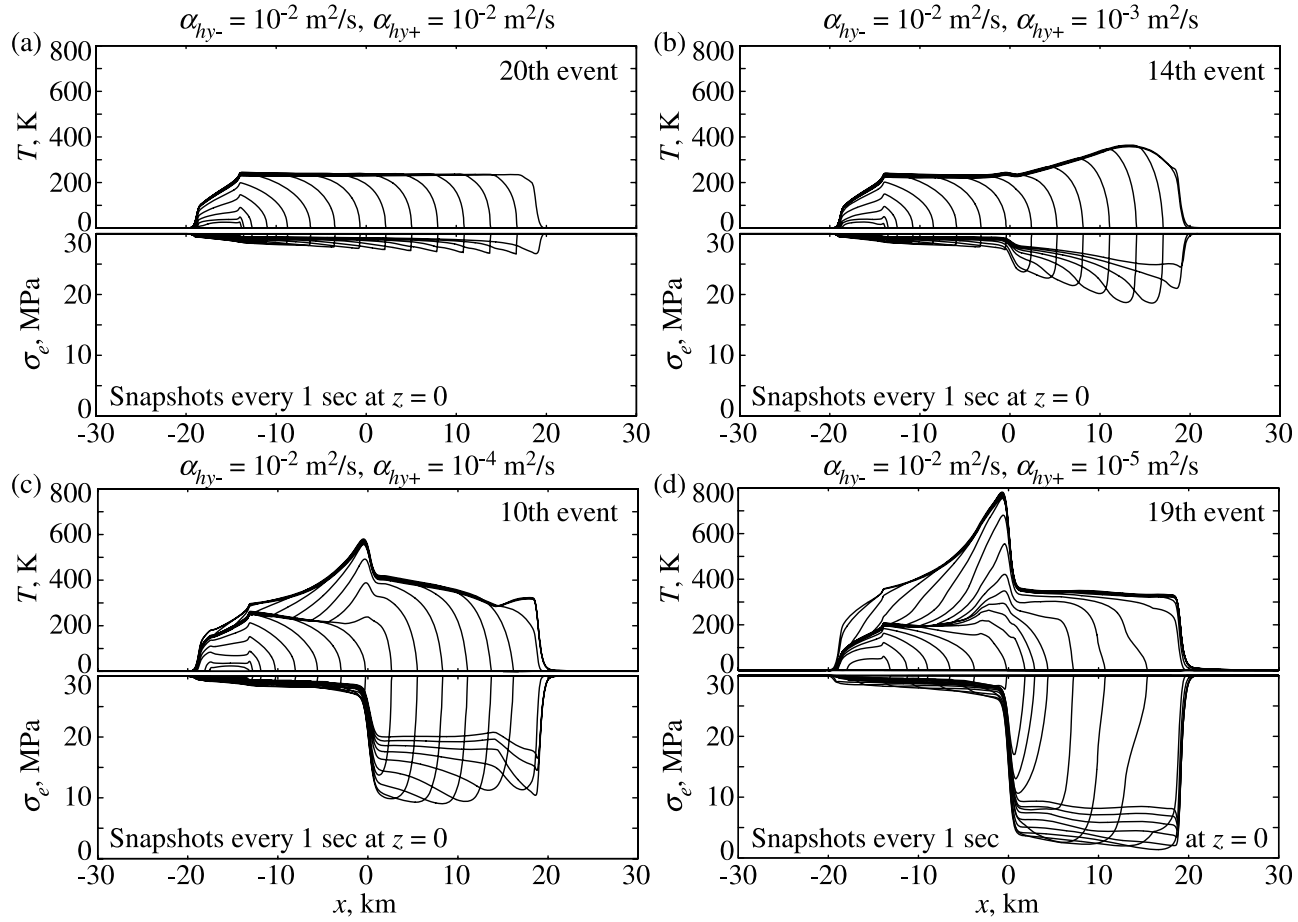

Figure 14. Snapshots of the temperature increase $T(x, y = 0, z = 0)$ and effective normal stress $\sigma_e(x, y = 0, z = 0)$ every 1 s during the model-spanning events marked in Figures 5a, 6a, 7, 8, 9, and 10. The location of the maximum temperature increase does not have the maximum slip. This is because the maximum slip occurs in the region with lower σ_e (see Figure 7).

This indicates that efficient TP may explain low heat generation along mature faults such as San Andreas [e.g., *Lachenbruch*, 1980].

4.4.2. Different Locations of Maximum Slip and Maximum Temperature Increase

[58] Intuitively, one would expect that the maximum temperature increase along seismogenic faults would occur at the locations of the largest slip, based on models in which the fault strength does not vary appreciably with the fault slip. In our models with heterogeneous hydraulic diffusivity, the highest slip is reached at the locations with the lowest stress, and hence it is not clear what the relation between the slip and the temperature increase would be. To understand that relation, we plot (Figure 14) snapshots of the temperature $T(x, z = 0)$ and the effective normal stress $\sigma_e(x, z = 0)$ during the same events as in Figure 11. Indeed, we find that if the heterogeneity in α_{hy} is strong enough, the maximum temperature rise during a model-spanning event is achieved between the patches (at slightly negative x), and not in the patch with more efficient TP which produces larger slip. As indicated by the series of snapshots in Figures 14c and 14d, the backward rupture propagation discussed in section 4.4.1 significantly contributes to the temperature increase in the region of less efficient TP. For the cases with $\alpha_{hy-} = 10^{-2}$ m^2/s and $\alpha_{hy+} = 10^{-2}$ and 10^{-3} m^2/s, the distribution of T is more or less uniform in the ruptured area.

[59] Such distribution of the temperature increase can be explained if we consider both the slip distribution and fault weakening. If $\alpha_{hy+} = 10^{-2}$ m^2/s, the decrease in the effective stress due to the build up in pore pressure p is at most about 0.1 of σ_{e0} (Figure 14a). For smaller α_{hy}, p increases, and hence the effective normal stress decreases, more significantly (Figures 14b, 14c, and 14d). The more significant dynamic weakening causes larger slip but their combination results in smaller heat generation as discussed in section 4.4.1, and hence smaller temperature increase. The slip associated with the backward rupture propagation, while much smaller, causes a comparable temperature increase due to much higher fault resistance.

[60] Note that a thinner shear zone (smaller w) would cause a higher temperature rise. Figure 15 shows the sequence of earthquakes and the temperature rise during one of the model-spanning events (indicated by an arrow in Figure 15a) for the case with $\alpha_{hy-} = 10^{-2}$ m^2/s, $\alpha_{hy+} = 10^{-4}$ m^2/s, and $w = 5$ mm. The maximum temperature rise in this case is higher than 1000 K which should cause melting. Since the fault constitutive law assumed in this work does not incorporate melting, we have chosen the

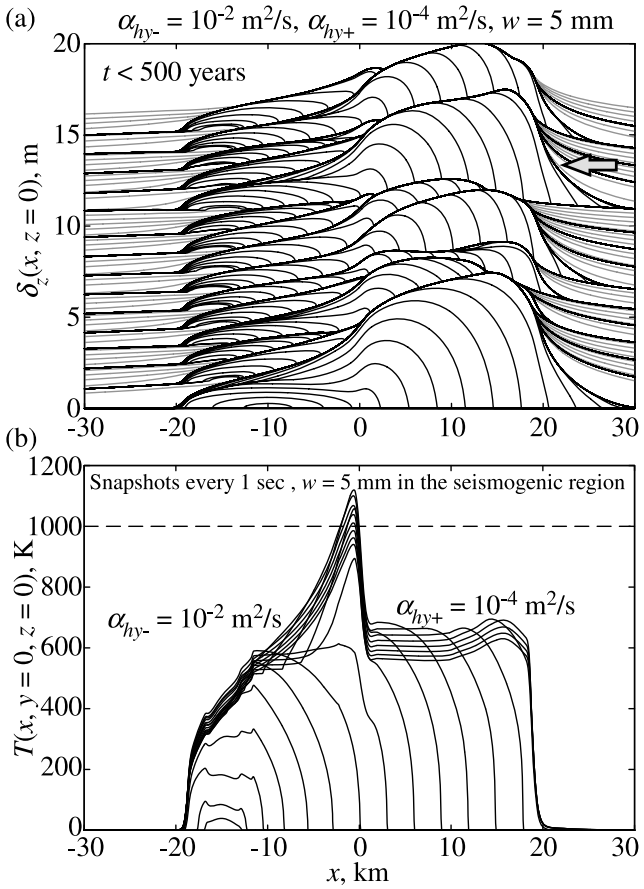

Figure 15. (a) Slip accumulation and (b) temperature rise during one of the model-spanning event in the case with $\alpha_{hy-} = 10^{-2}$ m^2/s, $\alpha_{hy+} = 10^{-4}$ m^2/s, and $w = 5$ mm. A thinner shear zone causes larger temperature rise, which would cause melting.

size of the fault, the effective normal stress for $p = 0$, and the width w of the shear zone so that the maximum temperature never reaches 1000 K in our simulations.

4.5. Earthquake Nucleation in the Region of Less Efficient TP

[61] *Segall and Rice* [2006] investigated the effect of TP on rupture nucleation, showing that efficient TP promotes nucleation by decreasing the nucleation size (or the critical stiffness). The critical stiffness for the undrained and adiabatic limit is given by [*Segall and Rice*, 2006]

$$k_{uaw} = \sigma_e \left[\frac{b-a}{L} + \frac{\Lambda}{\rho c \sqrt{2\pi w}} \right], \qquad (42)$$

where $(b - a) > 0$. With our selection of the physical properties, the second, TP-related, term in equation (42) increases the critical stiffness by the factor of 2.5 in comparison with the one for the standard rate-and-state friction, which is $\sigma_e(b - a)/L$. Note that equation (42) is derived assuming no diffusion of heat or pore pressure from the fault and hence provides an upper bound for the effectiveness of TP in assisting the nucleation.

[62] We find that all seismic events in our model nucleate in the patch with higher hydraulic diffusivity and hence less efficient TP. This is because that patch has higher interseismic shear stress, while the study of *Segall and Rice* [2006] assumed uniform initial conditions. Seismic events in our model nucleate close to the creeping, velocity-strengthening zones. During interseismic period, creeping motion penetrates into the seismogenic patches (Figure 4, bottom row), driven by the stress concentration at its tip. If the width of the region creeping within the seismogenic zone becomes comparable to the nucleation size, slip accelerates into an earthquake as shown in Figure 4 (top row). The penetration of creeping motion takes place in both patches, but its width is typically narrower in the patch of lower α_{hy} than in the patch of higher α_{hy} (Figure 4, bottom row), due to the different levels of the interseismic shear stress in the two patches (Figure 10). That is why, despite the smaller nucleation size in the patch with more efficient TP, the simulated earthquakes in our model always nucleate in the patch with less efficient TP, as the latter has higher interseismic stress.

[63] Since there is some penetration of creep into the region of more efficient TP as well, it may be possible to achieve earthquake nucleation there for a different set of the hydraulic properties that promote nucleation even more. However, such changes in hydraulic properties may lead to other changes, such as even lower interseismic stress in that region. Further parameter study in the context of earthquake sequences is required to systematically address this problem.

[64] Note that in all simulations so far, the initial perturbation in stress was positioned so that the first event initiates in the left patch, which has less efficient TP in the cases with heterogeneous hydraulic properties. This is also

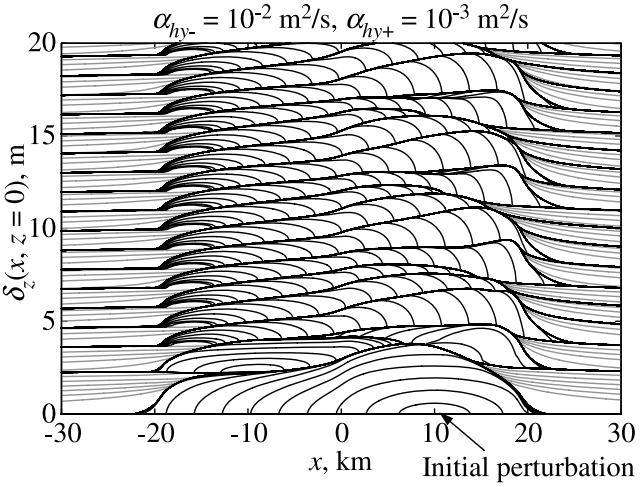

Figure 16. Slip accumulation on the fault with the same properties as those in the case of Figure 7c ($\alpha_{hy-} = 10^{-2}$ m^2/s, $\alpha_{hy+} = 10^{-3}$ m^2/s) but with the initial stress perturbation located in a different place (centered at $x = 10$ km and $z = -5$ km, versus $x = -10$ km and $z = -5$ km in the case of Figure 7c). The first event nucleates in the patch with more efficient TP because of the modified initial condition, but the following ones nucleate in the patch with less efficient TP, as in all previous cases.

the preferred location for all subsequent events. Hence we need to check that the location of the initial stress perturbation does not effect our conclusions about nucleation locations. Figure 16 presents a sequence of earthquakes with $\alpha_{hy-} = 10^{-2}$ m^2/s, $\alpha_{hy+} = 10^{-3}$ m^2/s, and the initial stress perturbation centered at $x = 10$ km and $z = -5$ km. The first event indeed nucleates in the right patch, responding to the initial stress distribution. However, all subsequent events still nucleate in the left patch, as before, demonstrating that the preferred location of nucleation in our model is indeed the effect of heterogeneous α_{hy}, and the associated heterogeneity in the interseismic shear stress, and not the effect of the initial stress condition.

[65] As a side note, in the cases with $\alpha_{hy-} = \alpha_{hy+}$, there is no heterogeneity and yet events keep nucleating at the same side of the fault as the first nucleation due to the initial stress perturbation. This is because ruptures accelerate and cause slightly larger slip and stress drop away from the nucleation region, due to inertial effects, even for the fault with the uniform physical properties. This is why the side of the fault that nucleates a seismic event has more favorable stress before the next seismic event, keeping the nucleation on the same side of the fault.

5. Conclusions

[66] We have developed a methodology for simulating earthquake sequences that accounts for the evolution of temperature and pore pressure on the fault due to frictional heating, including 1-D diffusion off the fault. The diffusion equations for temperature and pore pressure are integrated in time using a spectral method with a Fourier basis. This newly developed diffusion solver is unconditionally stable and computationally affordable. It is highly suitable for earthquake sequence simulations in which time steps are taken adaptively and vary by orders of magnitude. The methodology continues to account for inertial effects during seismic events, as in prior studies [*Lapusta and Liu*, 2009]. We have proposed several improvements in the numerical integration scheme.

[67] The effect of heterogeneous hydraulic diffusivity on long-term fault behavior and features of individual events have been examined by simulating the interaction of two fault patches. If the two patches have the same properties, the model behavior is simple, with only one characteristic model-spanning event. The earthquake sequences become more complex as heterogeneity in hydraulic diffusivity, motivated by field and laboratory measurements, is introduced. The patch with the more efficient thermal pressurization experiences larger coseismic slip when it ruptures, due to dynamic weakening. It does not rupture in every event and maintains much lower interseismic stress than the static frictional strength. The slip deficit in the other patch is filled with more frequent smaller events.

[68] In model-spanning events, the highest temperature increase does not occur in the area of the largest slip, as one would intuitively expect based on models in which there is no substantial dynamic weakening. The largest slip is experienced by the region with the more efficient thermal pressurization, and hence much of slip there occurs at a low, dynamically weakened, value of shear stress. This limits the temperature increase there in comparison with the fault areas right next to the area of the largest slip, which have somewhat lower slip but much higher shear stress. It is these areas, right next to the region of more efficient thermal pressurization, that experience the largest temperature increase. The temperature increase is further promoted there by backward rupture propagation, which occurs due to stress concentration caused by the area of rapid large slip. One of the implications is that if the hydraulic properties are heterogeneous along a fault, with some areas efficiently weakening during a large seismic event while the neighboring regions maintain relatively high friction resistance, it is possible that those neighboring regions would experience fault melting.

[69] We find that the dynamic events persistently nucleate in the patch of less efficient thermal pressurization, despite the fact that the theoretical estimate of the nucleation size is larger in that region [*Segall and Rice*, 2006]. This is because the interseismic shear stress there is much higher. We cannot exclude that the earthquake locations may change for a different parameter regime. In general, there would be a competition between the level of interseismic shear stress, which is higher inregions of less efficient pore pressurization, and the nucleation size, which is larger there and hence more difficult to achieve. However, one observation provides a hint that natural faults may also tend to have nucleation in places of less efficient TP. In our models, earthquake hypocenters are away from areas of the largest slip, since the hypocenters occur in the patch with less efficient TP and the largest slip occurs in the patch with more efficient TP. Such difference in the location of the hypocenters and areas of largest slip is also true for many earthquakes [see *Manighetti et al.*, 2005, Figure 12].

[70] The result on the nucleation locations highlights the importance of considering the effect of heterogeneity in fault properties on fault slip in the context of long-term simulations. This is because the heterogeneity eventually results in characteristic features of stress state on the fault, and it is the combination of the heterogeneous strength and stress that determines the fault behavior. This effect cannot be captured in considerations of a single nucleation instance or a single dynamic rupture on a heterogeneous fault.

[71] The methodology developed in this work provides an important tool for studies of relatively realistic coseismic fault behavior, with substantial physically motivated dynamic weakening and its interaction with fault heterogeneity and aseismic slip. An important next step would be to incorporate other known mechanisms that affect fault resistance to slip, such as melting [*Sirono et al.*, 2006; *Nielsen et al.*, 2008], reaction-related pore pressurization [*Sulem and Famin*, 2009], temperature dependency of the conventional rate- and state-dependent friction law [*Chester*, 1994; *Blanpied et al.*, 1998; *Noda*, 2008], and flash heating [*Rice*, 1999, 2006; *Beeler et al.*, 2008; *Noda*, 2008; *Bizzarri*, 2009].

Appendix A: Diffusion Solver

[72] Here we present a detailed error analysis of the diffusion solver presented in section 2.3. The test problem considered here is the same as in section 2.2, the diffusion response equation (19) of a quantity Q to a constant coseismic heat input (19). Our spectral method has three numerical parameters, l_{max}, l_{min}, and $\Delta\ln(l)$. As discussed in

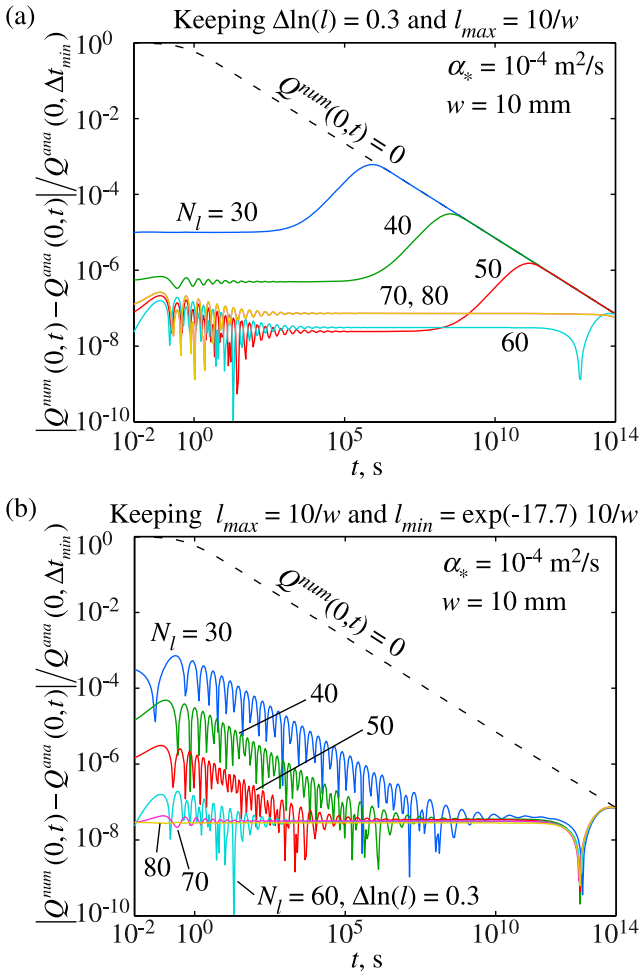

Figure A1. Comparison between the analytical solution to the test problem and the numerical solution based on the diffusion solver developed in this study. The difference between the two solutions is normalized by the maximum analytical value of the diffusing quantity Q.

section 2.2, we adopt $l_{\max} = 10/w$ because the contribution from the components with $|l| > 10/w$ is well below the round-off error of the double precision. Here we explore the effect of the other two parameters, $l_{\min}$ and $\Delta\ln(l)$. Figure A1 compares the numerical and analytical solutions by plotting their difference on the fault ($y = 0$), $|Q^{num}(0, t) - Q^{ana}(0, t)|$, normalized by the maximum coseismic value of Q, $Q^{ana}(0, \Delta t_{\min})$, for a range of values of $l_{\min}$ (Figure A1a) and $\Delta\ln(l)$ (Figure A1b), Different parameter values are indicated by N_l, the number of discretization points between $l_{\max}$ and $l_{\min}$. For reference, we plot $Q^{num}(0, t) = 0$ (black line) to show how the error would look if the numerical solution were identically zero at all times. As $l_{\min}$ decreases, the difference between the numerical and analytical solutions decreases, and the difference stays smaller for a longer time. As $\Delta\ln(l)$ decreases, the difference (numerical error) also decreases, but the decrease eventually saturates. This is because $Q^{ana}(0, t)$ can be approached only by decreasing both $l_{\min}$ and $\Delta\ln(l)$ at the same time, but $l_{\min}$ is kept constant in Figure A1b. The virtue of the method used in this study is the exponential convergence. As Figure A1b shows, the numerical error decreases exponentially due to a linear increase in N_l.

[73] Based on this parameter study, we choose $\Delta\ln(l) = 0.3$ and $N_l = 60$, which corresponds to $l_{\min} = 2.06 \times 10^{-7}/w$. The comparison between the analytical and numerical solutions for this case is shown in Figure 2. The chosen parameters correspond to numerical error well below 10^{-6} of the coseismic values. Q here stands for either temperature T or combination of temperature and pore pressure ($p + \Lambda' T$). The coseismic temperature rise is of the order of 100 K which corresponds to pore pressure rise of the order of $\Lambda' \times 100$ K $= \alpha_{th}/(\alpha_{hy} - \alpha_{th})10$ MPa. This is much smaller than 10 MPa because α_{hy} is larger than α_{th} by orders of magnitude in this study. The coseismic pore pressure rise is at most 30 MPa. Hence the relative error of 10^{-6} in either of those quantities would affect stress with values of order of 10 Pa, which is comparable to the accuracy of out Newton-Raphson method. There, we choose 10^{-6} as relative error in stress.

Appendix B: Comparison of Stability Between Two Integration Procedures for the State Variable Evolution

[74] In this work, we use a different numerical integration of the state variable evolution than the one in *Lapusta et al.* [2000] and *Lapusta and Liu* [2009]. Here we study the difference in the stability between the two time-integration schemes by considering which one would allow us to take larger time steps in a numerically stable way. For $V\Delta t/L > 10^{-6}$, our numerical integration of the state evolution is based on a constant value of V throughout the time step:

$$\theta(t_{n+1}) = \theta_{ss}(V(t_n)) + (\theta(t_n) - \theta_{ss}(V(t_n)))e^{\left(-\frac{V(t_n)\Delta t}{L}\right)}, \qquad \text{(B1)}$$

while *Lapusta et al.* [2000] used the approach based on constant θ,

$$\theta(t_{n+1}) = \theta(t_n) + \frac{V(t_n)\Delta t}{L}(\theta_{ss}(V(t_n)) - \theta(t_n)). \qquad \text{(B2)}$$

Lapusta et al. [2000] noted that one way to constrain numerical time steps is to consider linearized stability of steady sliding of the discretized system and, in particular, of perturbed motion of a single cell while the other cells continue steady sliding at a given slip rate. If the grid is properly refined, then the perturbation on a single cell dies away. Demanding that the time discretization preserves this property, we get a condition for the size of the time step allowed. The equation of motion for the single cell is equivalent to that for a spring-slider system, with the spring stiffness representing the effective elastic stiffness of the cell. *Lapusta et al.* [2000] conducted such analysis for the quasi-static motion and integration scheme (B2). Here we perform such analysis for both integration schemes, (B1) and (B2), and for both quasi-static and quasi-dynamic situations.

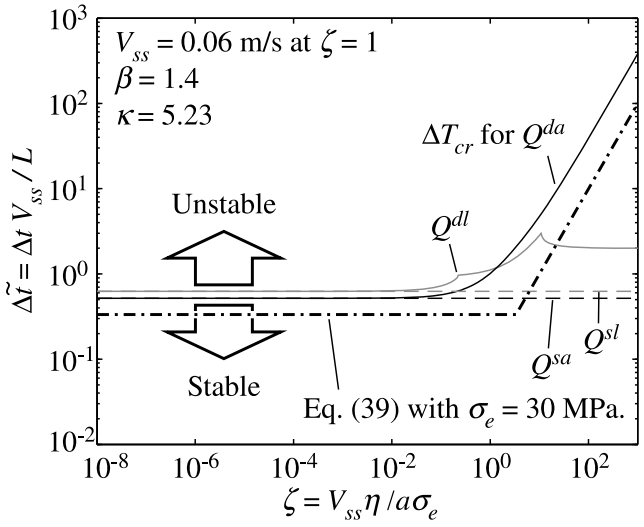

Figure B1. Stability criteria for numerical integration of quasi-static (dashed lines) and quasi-dynamic (thin solid lines) spring-slider models based on constant state evolution rate (gray lines) and constant slip rate (thin black lines). The choice of time stepping used in this work is indicated by a dot-dashed thick black line. Time integration scheme based on constant slip rate is more stable at coseismically high slip rates in terms of $\Delta\tilde{t}$.

[75] After linearization around a steady state solution with $V = V_{ss}$ and nondimensionalization using L as the characteristic length, V_{ss} as the characteristic velocity, and $a\sigma_e$ as the characteristic stress, the rate-and-state friction law becomes

$$\begin{aligned} \tilde{\tau} &= \tilde{V} + \beta\tilde{\theta}, \\ \tilde{\theta}' &= -\tilde{V} - \tilde{\theta}, \end{aligned} \tag{B3}$$

where $\sim$ denotes nondimensional quantities, $\beta = b/a$, and $'$ represents the derivative with respect to the nondimensional time, tV_{ss}/L. The equation of motion for the quasi-static spring-slider model is

$$\tau = K(V_{ss}t - \delta), \tag{B4}$$

where K is the spring constant. The linearized and nondimensional form of this equation is

$$\tilde{\tau} = -\kappa\tilde{\delta}, \tag{B5}$$

where $\kappa = KL/a\sigma_e$. Time evolution of slip $\tilde{\delta}$ is given by

$$\tilde{\delta}' = \tilde{V}. \tag{B6}$$

Numerical integration from t_n to t_{n+1}, over the nondimensional time step $\Delta\tilde{t}$ ($= \delta t V_{ss}/L$), yields

$$\begin{Bmatrix} \tilde{\delta}_{n+1} \\ \tilde{\theta}^{sl}_{n+1} \end{Bmatrix} = \begin{bmatrix} 1-\kappa\Delta\tilde{t} & -\beta\Delta\tilde{t} \\ \kappa\Delta\tilde{t} & 1+(\beta-1)\Delta\tilde{t} \end{bmatrix} \begin{Bmatrix} \tilde{\delta}_n \\ \tilde{\theta}_n \end{Bmatrix} = \mathbf{Q}^{sl}(\Delta\tilde{t}) \begin{Bmatrix} \tilde{\delta}_n \\ \tilde{\theta}_n \end{Bmatrix}. \tag{B7}$$

based on equation (B2) [*Lapusta et al.*, 2000] and

$$\begin{Bmatrix} \tilde{\delta}_{n+1} \\ \tilde{\theta}^{sa}_{n+1} \end{Bmatrix} = \begin{bmatrix} 1-\kappa\Delta\tilde{t} & -\beta\Delta\tilde{t} \\ \kappa\overline{\Delta\tilde{t}} & 1+(\beta-1)\overline{\Delta\tilde{t}} \end{bmatrix} \begin{Bmatrix} \tilde{\delta}_n \\ \tilde{\theta}_n \end{Bmatrix} = \mathbf{Q}^{sa}(\Delta\tilde{t}) \begin{Bmatrix} \tilde{\delta}_n \\ \tilde{\theta}_n \end{Bmatrix}, \tag{B8}$$

based on equation (B1), where $\overline{\Delta\tilde{t}} = 1 - e^{-\Delta\tilde{t}}$ and the superscripts ^{sl} and ^{sa} refer to the two state variable integration schemes. If the maximum absolute value of the eigenvalues of $\mathbf{Q}^{sl}$ $(\Delta\tilde{t})$ or $\mathbf{Q}^{sa}$ $(\Delta\tilde{t})$ is smaller than 1, then the perturbation on the single cell decays in the discretized case, just as we would expect in the continuous model. This gives a necessary condition to choose a proper $\Delta\tilde{t}$ for numerical stability [*Lapusta et al.*, 2000]. This quasi-static analysis is relevant to the stability of steady state sliding at low enough slip rates for the inertial effects to be negligible.

[76] Now let us formulate a one-degree of freedom model for the quasi-dynamic case,

$$\tau = K(V_{ss}t - \delta) - \eta V, \tag{B9}$$

which can be thought of as a spring-slider-dashpot model. This model is relevant to steady state sliding at slip rates high enough for the radiation damping term to be important (e.g., behind the front of a crack-like rupture, where slip often occurs nearly in steady state). The linearized equation of motion can be written as

$$\tilde{\tau} = -\kappa\tilde{\delta} - \zeta\tilde{V}, \tag{B10}$$

where $\zeta = \eta V_{ss}/a\sigma_e$. The evolution of perturbations based on equations (B1) and (B2) are now given by

$$\begin{Bmatrix} \tilde{\delta}_{n+1} \\ \tilde{\theta}^{dl}_{n+1} \end{Bmatrix} = \begin{bmatrix} 1-\dfrac{\kappa\Delta\tilde{t}}{1+\zeta} & -\dfrac{\beta\Delta\tilde{t}}{1+\zeta} \\ \dfrac{\kappa\Delta\tilde{t}}{1+\zeta} & 1+\left(\dfrac{\beta}{1+\zeta}-1\right)\Delta\tilde{t} \end{bmatrix} \begin{Bmatrix} \tilde{\delta}_n \\ \tilde{\theta}_n \end{Bmatrix} = \mathbf{Q}^{dl}(\Delta\tilde{t}) \begin{Bmatrix} \tilde{\delta}_n \\ \tilde{\theta}_n \end{Bmatrix}, \tag{B11}$$

and

$$\begin{Bmatrix} \tilde{\delta}_{n+1} \\ \tilde{\theta}^{da}_{n+1} \end{Bmatrix} = \begin{bmatrix} 1-\dfrac{\kappa\Delta\tilde{t}}{1+\zeta} & -\dfrac{\beta\Delta\tilde{t}}{1+\zeta} \\ \dfrac{\kappa\overline{\Delta\tilde{t}}}{1+\zeta} & 1+\left(\dfrac{\beta}{1+\zeta}-1\right)\overline{\Delta\tilde{t}} \end{bmatrix} \begin{Bmatrix} \tilde{\delta}_n \\ \tilde{\theta}_n \end{Bmatrix} = \mathbf{Q}^{da}(\Delta\tilde{t}) \begin{Bmatrix} \tilde{\delta}_n \\ \tilde{\theta}_n \end{Bmatrix}, \tag{B12}$$

respectively.

[77] To compare the values of $\Delta\tilde{t}$ that separate the growing and decaying behaviors of the perturbations, $\Delta\tilde{t}_{cr}$, for the two state variable integration schemes, we use the same the physical parameters and spatial grid size as in our simulation examples (section 4), which combine to give the following parameters: $\beta = b/a = 1.4$, $\kappa = \pi\mu L/4ha\sigma_e = 5.23$, and $a\sigma_e/\eta = 0.06$ m/s. The results, for both quasi-static and quasi-dynamic analyses, are plotted in Figure B1 as a

function of ζ. Note that the quasi-static case based on constant $\dot{\theta}$ allows for an analytical solution which was given by *Lapusta et al.* [2000]. We compute solutions for the other three cases numerically. The quasi-static analysis does not depend on ζ, and hence the results are given as straight horizontal lines. The two integration schemes are comparable in the quasi-static case, although the scheme based on the constant rate of state variable ($\mathbf{Q}^{sl}$) is slightly superior, in that it results in the slightly lower value of $\Delta\tilde{t}_{cr}$. Note that this is not the case for all parameter choices; for example, for a sparser spatial grid, with h = 100 m instead of 60 m, the scheme based on the constant slip rate ($\mathbf{Q}^{sa}$) becomes more stable (this result is not plotted). At slip rates low compared to ζ = 1 or V_{ss} = 0.06 m/s, there is little difference between the quasi-static and quasi-dynamic analyses, as should be the case, since the inertial effects are not important for such slip rates.

[78] As the slip rates (and hence ζ) increase, the stability region in terms of $\Delta\tilde{t}$ expands for both schemes in the quasi-dynamic analysis, but there is a significant difference between the two schemes. At coseismically high slip rates (e.g., ζ = 100 or V_{ss} = 6 m/s), $\Delta\tilde{t}_{cr}$ is more than 1 order of magnitude larger for the scheme based on the constant slip rate ($\mathbf{Q}^{da}$) than for the other scheme ($\mathbf{Q}^{dl}$). At the limit of an infinitely large slip rate, we get

$$\lim_{\zeta\to\infty}\mathbf{Q}^{dl}(\Delta\tilde{t}) = \begin{bmatrix} 1 & 0 \\ 0 & 1-\Delta\tilde{t} \end{bmatrix}, \tag{B13}$$

and

$$\lim_{\zeta\to\infty}\mathbf{Q}^{da}(\Delta\tilde{t}) = \begin{bmatrix} 1 & 0 \\ 0 & 1-\overline{\Delta\tilde{t}} \end{bmatrix}. \tag{B14}$$

Since $0 < \overline{\Delta\tilde{t}} < 1$, $\mathbf{Q}^{da}$ approaches an unconditionally stable operator. This is a very useful feature to have in dynamic rupture simulations, where slip rates at rupture tips can briefly reach very high values. While our analysis is not fully applicable to that case, as it considers perturbations from steady state sliding, this is still an encouraging result.

[79] The adaptive time step (equation (39)) that we employ in this work is indicated by a dot-dashed thick black line in Figure B1. Note that the line is within the stable region for both integration schemes, up until slip rates of the order of 0.6 m/s (ζ = 10). For higher slip rates, the time stepping used is within the stable regime for the scheme based on constant slip rate used in this work but not the other scheme.

Appendix C: Second-Order Accuracy of the State Variable Integration

[80] *Lapusta et al.* [2000], *Lapusta and Liu* [2009], and the present work use different methods of integrating θ. Consider the following updating methods:

$$\theta(\hat{t}+\Delta\hat{t}) = \theta(\hat{t}) + \frac{V_c\Delta\hat{t}}{L}(\theta_{ss}(V_c)-\theta_c), \tag{C1}$$

$$\theta(\hat{t}+\Delta\hat{t}) = \theta_{ss}(V_c) + (\theta(\hat{t})-\theta_{ss}(V_c))e^{\left(-\frac{V_c\Delta\hat{t}}{L}\right)}, \tag{C2}$$

and

$$\theta(\hat{t}+\Delta\hat{t}) = \theta(\hat{t}) + \frac{V_c\Delta\hat{t}}{L}(\theta_{ss}(V_c)-\theta(\hat{t})). \tag{C3}$$

Lapusta et al. [2000] used equation (C1), *Lapusta and Liu* [2009] used either equations (C2) or (C3), depending on the value of $V\theta/L$, and the present work uses either equations (C1) or (C2). Appendix C shows that the integration scheme after two iterations is second-order accurate for equations (C1) or (C2) but not for equation (C3).

[81] Let us assume that there exist smooth exact solutions, $V_{ex}(t)$ and $\theta_{ex}(t)$, to which our numerical solutions should converge as time steps decrease. V_{ex} and θ_{ex} satisfy

$$\frac{d\theta_{ex}}{dt}(t) = \frac{V_{ex}(t)}{L}(\theta_{ss}(V_{ex}(t))-\theta_{ex}(t)). \tag{C4}$$

Without loss of generality, let us consider integrating θ from $t = 0$ to $t = \Delta t$ given the initial conditions, $V_{ex}(0) = V_i$ and $\theta_{ex}(0) = \theta_i$. $V_{ex}(\Delta t)$ is represented by

$$V_{ex}(\Delta t) = V_i + A_i\Delta t + o(\Delta t^2), \tag{C5}$$

where A_i is the initial acceleration. $\theta_{ex}(\Delta t)$ is represented by

$$\theta_{ex}(\Delta t) = \theta_i + \frac{V_i}{L}(\theta_{ssi}-\theta_i)\Delta t + \frac{1}{2}\left[\frac{A_i}{L}(\theta_{ssi}-\theta_i) + \frac{V_iA_i}{L}\theta'_{ssi} - \frac{V_i^2}{L^2}(\theta_{ssi}-\theta_i)\right]\Delta t^2 + o(\Delta t^3). \tag{C6}$$

where $\theta_{ssi} = \theta_{ss}(V_i)$ and $\theta'_{ssi} = \theta'_{ss}(V_i)$.

[82] The two-iteration scheme used in this work is as follows.

[83] 1. From the initial value $\theta(0) = \theta_i$, advance time by Δt using $V_c = V_i$ and $\theta_c = \theta_i$. The result is denoted $\theta^*(\Delta t)$.

[84] 2. From the initial value $\theta(0) = \theta_i$, advance time by $\Delta t/2$ using $V_c = V_i$ and $\theta_c = \theta_i$. Let us denote the result by $\theta_{1/2}$.

[85] 3. From the initial value $\theta(\Delta t/2) = \theta_{1/2}$, advance time by $\Delta t/2$ using the first predictions of V and θ at $t = \Delta t$, which are $V^*(\Delta t)$ and $\theta^*(\Delta t)$. The results are denoted by $\theta^{**}(\Delta t)$ and adopted as the value at the time $t = \Delta t$.

[86] Let us assume that the computation of the functional term and the Newton-Raphson search is accurate enough so that $V^*(\Delta t)$ is first-order accurate:

$$V^*(\Delta t) = V_i + A_i\Delta t + o(\Delta t^2). \tag{C7}$$

If $\theta^{**}(\Delta t)$ is calculated using equations (C1)–(C3), equations (C1) and (C2) result in

$$\theta^{**}(\Delta t) = \theta_i + \frac{V_i}{L}(\theta_{ssi}-\theta_i)\Delta t + \frac{1}{2}\left[\frac{A_i}{L}(\theta_{ssi}-\theta_i) + \frac{V_iA_i}{L}\theta'_{ssi} - \frac{V_i^2}{L^2}(\theta_{ssi}-\theta_i)\right]\Delta t^2 + o(\Delta t^3). \tag{C8}$$

Comparing with the expansion of the exact solution, equation (C6), we conclude that the schemes equations (C1) and (C2) are second-order accurate in the adopted two-iteration scheme. However, equation (C3) yields

$$\theta^{**}(\Delta t) = \theta_i + \frac{V_i}{L}(\theta_{ssi}-\theta_i)\Delta t + \frac{1}{2}\left[\frac{A_i}{L}(\theta_{ssi}-\theta_i) + \frac{V_iA_i}{L}\theta'_{ssi}\right]\Delta t^2 + o(\Delta t^3), \tag{C9}$$

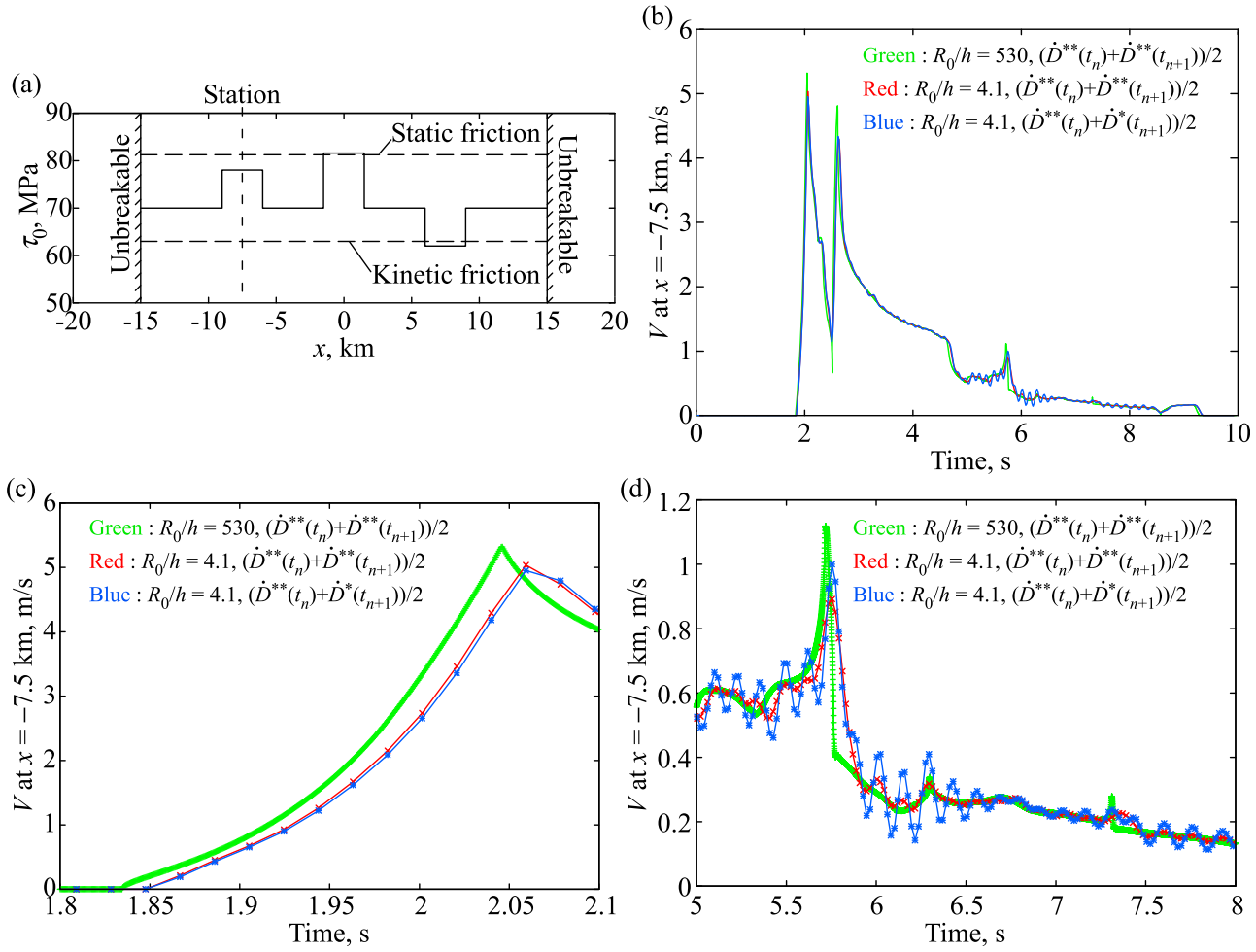

Figure C1. Comparison of numerical solutions with different approaches to convolution storage history. (a) Distribution of initial shear stress and static and kinetic frictional resistance in a test problem, TPV205-2D [*Harris et al.*, 2009]. (b) Numerical solutions for the slip rate history at x = −7.5 km with different resolutions and choice of history to be stored, as explained in the text. (c and d) Close-ups of the solutions at the rupture front and tail, respectively.

which is only first-order accurate approximation to $\theta_{ex}(\Delta t)$.

Appendix D: Comparison of Two Numerical Schemes With Different Storage for Computing Convolutions

[87] Previous studies [*Lapusta et al.*, 2000; *Lapusta and Liu*, 2009] stored the values $(\dot{D}^{**}(t_n) + \dot{D}^{*}(t_{n+1}))/2$ as the history for $t_n < t < t_{n+1}$, for use in computing dynamic stress transfers. This work uses $(\dot{D}^{**}(t_n) + \dot{D}^{**}(t_{n+1}))/2$. Here we compare the performance of the two algorithms using a 2-D dynamic rupture simulation problem TPV205-2D defined by the SCEC/USGS Spontaneous Rupture Code Verification Project [*Harris et al.*, 2009].

[88] In the problem, a 2-D in-plane dynamic rupture propagates on a 30-km long fault governed by a linear slip-weakening law. The fault prestress is heterogeneous, as shown in Figure C1a. Letting x be a coordinate along the fault, the initial shear stress τ_0 is 81.6 MPa for −1.5 km < x < 1.5 km, 78 MPa for −9 km < x < −6 km, 62 MPa for 6 km < x < 9 km, and 70 MPa otherwise. There are unbreakable barriers at $|x|$ = 15 km. The static and dynamic friction strength is 81.24 MPa and 63 MPa, respectively, and the slip weakening distance is 0.4 m. The P and S wave speeds are 6000 m/s and 3464 m/s, respectively, and the density is 2670 kg/m^3. The slip-weakening rate is 45.6 MPa/m and the quasi-static cohesive zone size R_0 is 828 m.

[89] Figures C1b, C1c, and C1d compare numerical solutions for the slip rate history at x = −7.5 km obtained in 3 different simulations. The very well-resolved solution (green) uses h = 1.5625 (resulting in R_0/h = 530) and $(\dot{D}^{**}(t_n) + \dot{D}^{**}(t_{n+1}))/2$ for history storage. The other two solutions (red and blue) use $(\dot{D}^{**}(t_n) + \dot{D}^{**}(t_{n+1}))/2$ and $(\dot{D}^{**}(t_n) + \dot{D}^{*}(t_{n+1}))/2$, respectively, with a much lower resolution h = 200 m (R_0/h = 4.1) which is comparable to what is used in the main part of this study.

[90] Although the overall behavior is reasonably resolved with R_0/h = 4.1 by both algorithms (Figure C1b), the one used in this study (with $(\dot{D}^{**}(t_n) + \dot{D}^{**}(t_{n+1}))/2$

for history storage) performs better. First, the rupture arrival is slightly earlier and closer to the well-resolved solution (Figure C1c). Second, numerical oscillations are less significant (Figure C1d). Therefore, we conclude that it is better to use $(\dot{D}^{**}(t_n) + \dot{D}^{**}(t_{n+1}))/2$ for history storage.

[91] **Acknowledgments.** This study was supported by National Science Foundation grant EAR 0548277, U.S. Geological Survey grant 08HQGR0057, and Southern California Earthquake Center (SCEC). SCEC is funded by NSF Cooperative Agreement EAR-0106924 and USGS Cooperative Agreement 02HQAG0008. This is SCEC contribution 1432. The numerical simulations for this research were performed on Caltech Division of Geological and Planetary Sciences Dell cluster. We thank Toshihiko Shimamoto and Wataru Tanikawa for discussions on their geological observations. We thank Associate Editor Robert Nowack and reviewers Andrea Bizzarri and Takehito Suzuki for detailed comments that improved this paper.

References

Andrews, D. J. (2002), A fault constitutive relation accounting for thermal pressurization of pore fluid, *J. Geophys. Res.*, *107*(B12), 2363, doi:10.1029/2002JB001942.

Andrews, D. J. (2005), Thermal pressurization explains enhanced long-period motion in the Chi-Chi earthquake, *Eos Trans. AGU*, *86*(52), Fall Meet. Suppl., Abstract S34A-04.

Beeler, N. M., T. E. Tullis, M. L. Blanpied, and J. D. Weeks (1996), Frictional behavior of large displacement experimental faults, *J. Geophys. Res.*, *101*(B4), 8697–8715, doi:10.1029/96JB00411.

Beeler, N. M., T. E. Tullis, and D. L. Goldsby (2008), Constitutive relationships and physical basis of fault strength due to flash heating, *J. Geophys. Res.*, *113*, B01401, doi:10.1029/2007JB004988.

Bizzarri, A. (2009), Can flash heating of asperity contacts prevent melting?, *Geophys. Res. Lett.*, *36*, L11304, doi:10.1029/2009GL037335.

Bizzarri, A., and M. E. Belardinelli (2008), Modelling instantaneous dynamic triggering in a 3-D fault system: Application to the 2000 June south Iceland seismic sequence, *Geophys. J. Int.*, *173*, 906–921, doi:10.1111/j.1365-246X.2008.03765.x.

Bizzarri, A., and M. Cocco (2006a), A thermal pressurization model for the spontaneous dynamic rupture propagation on a three-dimensional fault: 1. Methodological approach, *J. Geophys. Res.*, *111*, B05303, doi:10.1029/2005JB003862.

Bizzarri, A., and M. Cocco (2006b), A thermal pressurization model for the spontaneous dynamic rupture propagation on a three-dimensional fault: 2. Traction evolution and dynamic parameters, *J. Geophys. Res.*, *111*, B05304, doi:10.1029/2005JB003864.

Blanpied, M. L., C. J. Marone, D. A. Lockner, J. D. Byerlee, and D. P. King (1998), Quantitative measure of the variation in fault rheology due to fluid-rock interactions, *J. Geophys. Res.*, *103*(B5), 9691–9712, doi:10.1029/98JB00162.

Brantut, N., A. Schubnel, J.-N. Rouzaud, F. Brunet, and T. Shimamoto (2008), High-velocity frictional properties of a clay-bearing fault gouge and implications for earthquake mechanics, *J. Geophys. Res.*, *113*, B10401, doi:10.1029/2007JB005551.

Chester, F. M. (1994), Effects of temperature on friction: Constitutive equations and experiments with quartz gouge, *J. Geophys. Res.*, *99*(B4), 7247–7261, doi:10.1029/93JB03110.

Chester, F. M., and J. S. Chester (1998), Ultracataclasite structure and friction processes of the Punchbowl fault, San Andreas system, California, *Tectonophysics*, *295*, 199–221, doi:10.1016/S0040-1951(98)00121-8.

Chester, F. M., J. S. Chester, D. L. Kirschner, S. E. Schulz, and J. P. Evans (2004), Structure of large-displacement, strike-slip fault zones in the brittle continental crust, in *Rheology and Deformation in the Lithosphere at Continental Margins*, edited by G. D. Karner et al., pp. 223–260, Columbia Univ. Press, New York.

Cocco, M., and A. Bizzarri (2004), Dynamic fault weakening caused by thermal pressurization in an earthquake model governed by rate- and state-dependent friction, *Eos Trans. AGU*, *85*(47), Fall Meet. Suppl., Abstract T22A-06.

Cochard, A., and J. R. Rice (2000), Fault rupture between dissimilar materials: Ill-posedness, regularization and slip-pulse response, *J. Geophys. Res.*, *105*(B11), 25,891–25,907, doi:10.1029/2000JB900230.

d'Alessio, M. A., A. E. Blythe, and R. Bürgmann (2003), No frictional heat along the San Gabriel fault, California: Evidence from fission track thermochronology, *Geology*, *31*(6), 541–544, doi:10.1130/0091-7613(2003)031<0541:NFHATS>2.0.CO;2.

Day, S. M., L. A. Dalguer, N. Lapusta, and Y. Liu (2005), Comparison of finite difference and boundary integral solutions to three-dimensional spontaneous rupture, *J. Geophys. Res.*, *110*, B12307, doi:10.1029/2005JB003813.

Dieterich, J. H. (1972), Time-dependent friction in rocks, *J. Geophys. Res.*, *77*(20), 3690–3697, doi:10.1029/JB077i020p03690.

Dieterich, J. H. (1979), Modeling of rock friction: 1. Experimental results and constitutive equations, *J. Geophys. Res.*, *84*(B5), 2161–2168, doi:10.1029/JB084iB05p02161.

Faulkner, D. R. (2004), A model for the variation in permeability of clay-bearing fault gouge with depth in the brittle crust, *Geophys. Res. Lett.*, *31*, L19611, doi:10.1029/2004GL020736.

Faulkner, D. R., and E. H. Rutter (2003), The effect of temperature, nature of the pore fluid, and subyield differential stress on the permeability of phyllosilicate-rich fault gouge, *J. Geophys. Res.*, *108*(B5), 2227, doi:10.1029/2001JB001581.

Fialko, Y. (2004), Temperature fields generated by the elastodynamic propagation of shear cracks in the Earth, *J. Geophys. Res.*, *109*, B01303, doi:10.1029/2003JB002497.

Fukuchi, T., K. Mizoguchi, and T. Shimamoto (2005), Ferrimagnetic resonance signal produced by frictional heating: A new indicator of paleoseismicity, *J. Geophys. Res.*, *110*, B12404, doi:10.1029/2004JB003485.

Fukuyama, E., and K. Mizoguchi (2010), Constitutive parameters for earthquake rupture dynamics based on high-velocity friction tests with variable slip rate, *Int. J. Fract.*, *163*, 15–26, doi:10.1007/s10704-009-9417-5.

Geubelle, P. H., and J. R. Rice (1995), A spectral method for three-dimensional elastodynamic fracture problems, *J. Mech. Phys. Solids*, *43*, 1791–1824, doi:10.1016/0022-5096(95)00043-I.

Hamada, Y., T. Hirono, M. Ikehara, W. Soh, and S. R. Song (2009a), Estimated dynamic shear stress and frictional heat during the 1999 Taiwan Chi-Chi earthquake: A chemical kinetics approach with isothermal heating experiments, *Tectonophysics*, *469*, 73–84, doi:10.1016/j.tecto.2009.01.036.

Hamada, Y., T. Hirono, W. Tanikawa, W. Soh, and S. R. Song (2009b), Energy taken up by coseismic chemical reactions during a large earthquake: An example from the 1999 Taiwan Chi-Chi earthquake, *Geophys. Res. Lett.*, *36*, L06301, doi:10.1029/2008GL036772.

Han, R., T. Shimamoto, T. Hirose, J.-H. Ree, and J. Ando (2007), Ultralow friction of carbonate faults caused by thermal decomposition, *Science*, *316*(5826), 878–881, doi:10.1126/science.1139763.

Harris, R. A., et al. (2009), The SCEC/USGS dynamic earthquake-rupture code verification exercise, *Seismol. Res. Lett.*, *80*(1), 119–126, doi:10.1785/gssrl.80.1.119.

Heermance, R., Z. K. Shipton, and J. P. Evans (2003), Fault structure control on fault slip and ground motion during the 1999 rupture of the Chelungpu Fault, Taiwan, *Bull. Seismol. Soc. Am.*, *93*(3), 1034–1050, doi:10.1785/0120010230.

Hickman, S., and M. Zoback (2004), Stress orientations and magnitudes in the SAFOD pilot hole, *Geophys. Res. Lett.*, *31*, L15S12, doi:10.1029/2004GL020043.

Hirono, T., et al. (2008), Clay mineral reactions caused by frictional heating during an earthquake: An example from the Taiwan Chelungpu fault, *Geophys. Res. Lett.*, *35*, L16303, doi:10.1029/2008GL034476.

Hirose, T., and T. Shimamoto (2005), Growth of a molten zone as a mechanism of slip weakening of simulated faults in gabbro during frictional melting, *J. Geophys. Res.*, *110*, B05202, doi:10.1029/2004JB003207.

Kano, Y., J. Mori, R. Fujio, H. Ito, T. Yanagidani, S. Nakao, and K. F. Ma (2006), Heat signature on the Chelungpu fault associated with the 1999 Chi-Chi, Taiwan earthquake, *Geophys. Res. Lett.*, *33*, L14306, doi:10.1029/2006GL026733.

Lachenbruch, A. H. (1980), Frictional heating, fluid pressure, and the resistance to fault motion, *J. Geophys. Res.*, *85*(B11), 6097–6112, doi:10.1029/JB085iB11p06097.

Lapusta, N., and Y. Liu (2009), Three-dimensional boundary integral modeling of spontaneous earthquake sequences and aseismic slip, *J. Geophys. Res.*, *114*, B09303, doi:10.1029/2008JB005934.

Lapusta, N., and J. R. Rice (2003), Low-heat and low-stress fault operation in earthquake models of statically strong but dynamically weak faults, *Eos Trans. AGU*, *84*(46), Fall Meet. Suppl., Abstract S51B-02.

Lapusta, N., J. R. Rice, Y. Ben-Zion, and G. Zheng (2000), Elastodynamic analysis for slow tectonic loading with spontaneous rupture episodes on faults with rate- and state-dependent friction, *J. Geophys. Res.*, *105*(B10), 23,765–23,789, doi:10.1029/2000JB900250.

Linker, M. F., and J. H. Dieterich (1992), Effects of variable normal stress on rock friction: Observations and constitutive equations, *J. Geophys. Res.*, *97*(B4), 4923–4940, doi:10.1029/92JB00017.

Ma, K. F., J. Mori, S. J. Lee, and S. B. Yu (2003), Spatial and temporal distribution of slip for the 1999 Chi-Chi, Taiwan, earthquake, *Bull. Seismol. Soc. Am.*, *93*, 264–282.

Manighetti, I., M. Campillo, C. Sammis, P. M. Mai, and G. King (2005), Evidence for self-similar, triangular slip distributions on earthquakes: Implications for earthquake and fault mechanics, *J. Geophys. Res.*, *110*, B05302, doi:10.1029/2004JB003174.

Mase, C. W., and L. Smith (1987), Effects of frictional heating on the thermal, hydrologic, and mechanical response of a fault, *J. Geophys. Res.*, *92*(B7), 6249–6272, doi:10.1029/JB092iB07p06249.

McKenzie, D., and J. N. Brune (1972), Melting on fault planes during large earthquakes, *Geophys. J. R. Astron. Soc.*, *29*, 65–78.

Mitsui, Y., and K. Hirahara (2009), Coseismic thermal pressurization can notably prolong earthquake recurrence intervals on weak rate and state friction faults: Numerical experiments using different constitutive equations, *J. Geophys. Res.*, *114*, B09304, doi:10.1029/2008JB006220.

Mizoguchi, K., and T. Shimamoto (2004), Dramatic slip weakening of Nojima fault gouge at high-velocities and its implication for dynamic fault motion, *Eos Trans. AGU*, *85*(47), Fall Meet. Suppl., Abstract T23A-0559.

Mizoguchi, K., T. Hirose, T. Shimamoto, and E. Fukuyama (2006), Moisture-related weakening and strengthening of a fault activated at seismic slip rate, *Geophys. Res. Lett.*, *33*, L16319, doi:10.1029/2006GL026980.

Mizoguchi, K., T. Hirose, T. Shimamoto, and E. Fukuyama (2007), Reconstruction of seismic faulting by high-velocity friction experiments: An example of the 1995 Kobe earthquake, *Geophys. Res. Lett.*, *34*, L01308, doi:10.1029/2006GL027931.

Nielsen, S. B., G. D. Toro, T. Hirose, and T. Shimamoto (2008), Frictional melt and seismic slip, *J. Geophys. Res.*, *113*, B01308, doi:10.1029/2007JB005122.

Noda, H. (2004), Numerical simulation of rupture propagation with thermal pressurization based on measured hydraulic properties: Importance of deformation zone width, *Eos Trans. AGU*, *85*(47), Fall Meet. Suppl., Abstract T22A-08.

Noda, H. (2008), Frictional constitutive law at intermediate slip rates accounting for flash heating and thermally activated slip process, *J. Geophys. Res.*, *113*, B09302, doi:10.1029/2007JB005406.

Noda, H., and T. Shimamoto (2005), Thermal pressurization and slip-weakening distance of a fault: An example of the Hanore fault, southwest Japan, *Bull. Seismol. Soc. Am.*, *95*(4), 1224–1233, doi:10.1785/0120040089.

Noda, H., E. M. Dunham, and J. R. Rice (2009), Earthquake ruptures with thermal weakening and the operation of major faults at low overall stress levels, *J. Geophys. Res.*, *114*, B07302, doi:10.1029/2008JB006143.

O'Hara, K., K. Mizoguchi, T. Shimamoto, and J. C. Hower (2006), Experimental frictional heating of coal gouge at seismic slip rates: Evidence for devolatilization and thermal pressurization of gouge fluids, *Tectonophysics*, *424*, 109–118, doi:10.1016/j.tecto.2006.07.007.

Perrin, G., J. R. Rice, and G. Zheng (1995), Self-healing slip pulse on a frictional interface, *J. Mech. Phys. Solids*, *43*, 1461–1495, doi:10.1016/0022-5096(95)00036-I.

Rempel, A. W., and J. R. Rice (2006), Thermal pressurization and onset of melting in fault zones, *J. Geophys. Res.*, *111*, B09314, doi:10.1029/2006JB004314.

Rice, J. R. (1992), Fault stress states, pore pressure distributions, and the weakness of the San Andreas Fault, in *Fault Mechanics and Transport Properties of Rocks*, edited by B. Evans and T.-F. Wong, pp. 475–503, Academic, San Diego, Calif., doi:10.1016/S0074-6142(08)62835-1.

Rice, J. R. (1993), Spatio-temporal complexity of slip on a fault, *J. Geophys. Res.*, *98*(B6), 9885–9907, doi:10.1029/93JB00191.

Rice, J. R. (1999), Flash heating at asperity contacts and rate-dependent friction, *Eos Trans. AGU*, *80*(46), Fall Meet. Suppl., F681l.

Rice, J. R. (2006), Heating and weakening of faults during earthquake slip, *J. Geophys. Res.*, *111*, B05311, doi:10.1029/2005JB004006.

Rice, J. R., N. Lapusta, and K. Ranjith (2001), Rate and state dependent friction and the stability of sliding between elastically deformable solids, *J. Mech. Phys. Solids*, *49*, 1865–1898, doi:10.1016/S0022-5096(01)00042-4.

Rice, J. R., E. M. Dunham, and H. Noda (2009), Thermo- and hydro-mechanical processes along faults during rapid slip, in *Meso-scale Shear Physics in Earthquake and Landslide Mechanics*, edited by Y. Hatzor, J. Sulem, and I. Vardoulakis, pp. 3–16, CRC Press, Boca Raton, Fla.

Schmitt, S. V., and P. Segall (2008), Shear heating-induced thermal pressurization during the nucleation of earthquakes, *Eos Trans. AGU*, *89*(53), Fall Meet. Suppl., Abstract T21-D-08.

Segall, P., and J. R. Rice (1995), Dilatancy, compaction, and slip instability of a fluid-infiltrated fault, *J. Geophys. Res.*, *100*(B11), 22,155–22,171, doi:10.1029/95JB02403.

Segall, P., and J. R. Rice (2006), Does shear heating of pore fluid contribute to earthquake nucleation?, *J. Geophys. Res.*, *111*, B09316, doi:10.1029/2005JB004129.

Sibson, R. H. (1973), Interaction between temperature and pore fluid pressure during earthquake faulting: A mechanism for partial or total stress relief, *Nature*, *243*, 66–68.

Sibson, R. H. (1975), Generation of pseudotachylyte by ancient seismic faulting, *Geophys. J. R. Astron. Soc.*, *43*, 775–794.

Sirono, S., K. Satomi, and S. Watanabe (2006), Numerical simulations of frictional melting: Small dependence of shear stress drop on viscosity parameters, *J. Geophys. Res.*, *111*, B06309, doi:10.1029/2005JB003858.

Sone, H., and T. Shimamoto (2009), Frictional resistance of faults during accelerating and decelerating earthquake slip, *Nat. Geosci.*, *2*, 705–708, doi:10.1038/ngeo637.

Sulem, J., and V. Famin (2009), Thermal decomposition of carbonates in fault zones: Slip-weakening and temperature-limiting effects, *J. Geophys. Res.*, *114*, B03309, doi:10.1029/2008JB006004.

Suppe, J., and J. H. Wittke (1977), Abnormal pore fluid pressures in relation to stratigraphy and structure in the active fold-and thrust belt of northwestern Taiwan, *Petrol. Geol. Taiwan*, *14*, 11–24.

Suzuki, T., and T. Yamashita (2006), Nonlinear thermoporoelastic effects on dynamic earthquake ruptures, *J. Geophys. Res.*, *111*, B03307, doi:10.1029/2005JB003810.

Suzuki, T., and T. Yamashita (2009), Dynamic modeling of slow earthquakes based on thermoporoelastic effects and inelastic generation of pores, *J. Geophys. Res.*, *114*, B00A04, doi:10.1029/2008JB006042.

Takagi, H., and K. Shibata (2000), Constituents of the paleo-Ryoke belt and restoration of the paleo-Ryoke and Kurosegawa terranes (geotectonic evolution of the paleo-Ryoke and Kurosegawa terranes) (in Japanese with English abstract), *Mem. Geol. Soc. Jpn.*, *56*, 1–12.

Tanaka, H., W. M. Chen, C. Y. Wang, K. F. Ma, N. Urata, J. Mori, and M. Ando (2006), Frictional heat from faulting of the 1999 Chi-Chi, Taiwan earthquake, *Geophys. Res. Lett.*, *33*, L16316, doi:10.1029/2006GL026673.

Tanikawa, W., and T. Shimamoto (2009), Frictional and transport properties of the Chelungpu fault from shallow borehole data and their correlation with seismic behavior during the 1999 Chi-Chi earthquake, *J. Geophys. Res.*, *114*, B01402, doi:10.1029/2008JB005750.

Tanikawa, W., T. Shimamoto, S. K. Wey, C. W. Lin, and W. C. Lai (2008), Stratigraphic variation of transport properties and overpressure development in the Western Foothills, Taiwan, *J. Geophys. Res.*, *113*, B12403, doi:10.1029/2008JB005647.

Terzaghi, K. (1936), The shearing resistance of saturated soils and the angle between the planes of shear, in *International Conference of Soil and Foundation Engineering*, pp. 54–56, Harvard Univ. Press, Cambridge, Mass.

Townend, J., and M. D. Zoback (2004), Regional tectonic stress near the San Andreas fault in central and southern California, *Geophys. Res. Lett.*, *31*, L15S11, doi:10.1029/2003GL018918.

Tsutsumi, A., and T. Shimamoto (1997), High velocity frictional properties of gabbro, *Geophys. Res. Lett.*, *24*(6), 699–702, doi:10.1029/97GL00503.

Tsutsumi, A., S. Nishino, K. Mizoguchi, T. Hirose, S. Uehara, K. Sato, W. Tanikawa, and T. Shimamoto (2004), Principal fault zone width and permeability of the active Neodani fault, Nobi fault system, southwest Japan, *Tectonophysics*, *379*, 93–108, doi:10.1016/j.tecto.2003.10.007.

Vredevoogd, M., D. Oglesby, and S. Park (2007), Effects of nonlinear terms and fault width on pore fluid pressurization, *Eos Trans. AGU*, *88*(52), Fall Meet. Suppl., Abstract S21B-0556.

Wibberley, C. A. J., and T. Shimamoto (2003), Internal structure and permeability of major strike-slip fault zones: The Median Tectonic Line in Mie Prefecture, southwest Japan, *J. Struct. Geol.*, *25*(1), 59–78, doi:10.1016/S0191-8141(02)00014-7.

Zheng, G., and J. R. Rice (1998), Conditions under which velocity-weakening friction allows a self-healing versus a cracklike mode of rupture, *Bull. Seismol. Soc. Am.*, *88*, 1466–1483.

N. Lapusta, Division of Geological and Planetary Sciences and Division of Engineering and Applied Science, California Institute of Technology, 1200 E. California Blvd., Mail Code 104-44, Pasadena, CA 91125, USA. (lapusta@its.caltech.edu)

H. Noda, Division of Geological and Planetary Sciences, California Institute of Technology, 1200 E. California Blvd., Mail Code 252-21, Pasadena, CA 91125, USA. (hnoda@caltech.edu)